

Contents lists available at ScienceDirect

## Petroleum Science

journal homepage: www.keaipublishing.com/en/journals/petroleum-science



# Original Paper

# Seismic pore-type characterization in tight carbonate reservoirs: A case study of the fourth member of Ordovician Majiagou Formation in Ordos Basin, China



Meng-Bo Zhang <sup>a,b</sup>, Hao-Jie Pan <sup>c,\*</sup>, Yong-Gang Wang <sup>a,b</sup>, Miao Du <sup>c</sup>, Sheng-Juan Cai <sup>d</sup>, Feng Liu <sup>a,b</sup>, Mei-Xin Ju <sup>a,b</sup>

- a National Engineering Laboratory for Exploration and Development of Low-permeability Oil and Gas Fields, Xi'an, 710018, Shaanxi, China
- <sup>b</sup> Research Institute of Petroleum Exploration and Development, PetroChina Changqing Oilfield Company, Xi'an, 710018, Shaanxi, China
- <sup>c</sup> College of Geophysics and Petroleum Resources, Yangtze University, Wuhan, 430100, Hubei, China

#### ARTICLE INFO

# Article history: Received 5 September 2024 Received in revised form 4 March 2025 Accepted 20 May 2025 Available online 22 May 2025

Edited by Meng-Jiao Zhou

Keywords: Carbonate reservoirs Pore type Rock physics model Seismic inversion Ordos Basin

#### ABSTRACT

Carbonate reservoirs are known for their complex pore structures, which lead to variable elastic behaviors and seismic responses. These variations pose significant challenges for seismic interpretation of carbonate reservoirs. Therefore, quantitative characterization of pore structure is crucial for accurate fluid detection and reservoir property estimation. To address the complexity of pore geometry and the uneven fluid distribution in tight carbonate reservoirs, we develop a triple-pore effective medium model by integrating the extended Keys-Xu model with the Gassmann-Hill equation. Comparison between the theoretical modeling results and an available laboratory data set verifies the effectiveness of this model in pore type quantification. Based on this calibrated model, we propose a novel two-step triple pore-type inversion strategy with varying pore aspect ratio via a grid-searching algorithm. We apply this method to well logs and 3D seismic data from the tight carbonate reservoirs of the Ordovician Majiagou formation in the Ordos Basin. The good agreement between pore-type estimates and logging interpretation results suggests that our method significantly improves the accuracy of porosity estimates for different pore types, outperforming the pore-type inversion method with fixed pore aspect ratios. The successful application to seismic data also demonstrates that the proposed method provides a reliable distribution of pore types in tight carbonate reservoirs, confirming its applicability and feasibility in seismic pore-type estimation. This method not only facilitates the recognition of complex pore geometries but also provides valuable insights for accurate detection of high-quality reservoirs. © 2025 The Authors. Publishing services by Elsevier B.V. on behalf of KeAi Communications Co. Ltd. This is an open access article under the CC BY-NC-ND license (http://creativecommons.org/licenses/by-ncnd/4.0/).

#### 1. Introduction

Carbonate reservoirs account for more than 50% of the global oil and gas reserves and hold significant exploration potential. Unlike conventional clastic reservoirs, carbonate reservoirs are characterized by complex pore structures due to various diagenetic processes such as cementation, compaction, dissolution, and dolomitization. These processes result in the formation of

E-mail address: panhaojie88@163.com (H.-J. Pan).

Peer review under the responsibility of China University of Petroleum (Beijing).

secondary pores and cracks (Anselmetti and Eberli, 1993). The pore systems in carbonate reservoirs often include vuggy pores, intragranular pores, intergranular pores, intercrystalline pores, and cracks (Zhao et al., 2013). Such complex pore structures significantly affect the permeability, acoustic properties, and seismic interpretation of carbonate reservoirs (Sun et al., 2006; Weger et al., 2009; Guo et al., 2023; Zhang et al., 2024). Therefore, accurately characterizing pore structures is crucial for assessing reservoir quality, describing reservoir architecture, and identifying sweet spots within carbonate reservoirs.

Efforts have been made to evaluate the pore structures of carbonate reservoirs. Experimental methods, such as thin-section analysis, computer tomography, scanning electron microscopy,

<sup>&</sup>lt;sup>d</sup> Resource Geophysics Academy, Imperial College London, SW7 2BP, London, UK

<sup>\*</sup> Corresponding author.

high-pressure mercury injection, and nuclear magnetic resonance, are effective in identifying complex pore structures (Tian et al., 2020; Sharifi, 2022). However, these methods are often limited by their discontinuous evaluations based on a small number of core samples. Additionally, they typically produce qualitative and subjective descriptions that are difficult to correlate with variations in elastic properties.

Well logging provides continuous evaluation of pore structure characteristics. For instance, the velocity deviation log is used to identify fractures and stiff pores by comparing measured velocities with those calculated using the Wyllie's time-average equation (Anselmetti and Eberli, 1999). Sonic and density logs can also be used to derive matrix porosity and total porosity through empirical relationships (Du et al., 2024). Nevertheless, log-based interpretations can only classify frame-forming pores and cracks or quantify the specific pore type, but face constraints in simultaneously evaluating multiple pore types at well locations (Wu and Chen, 2014; Sharifi et al., 2018; Saberi, 2020). Thus, there is an urgent need for methods that can simultaneously quantify the spatial distribution of multiple pore types within carbonate reservoirs

Pore aspect ratio, defined as the ratio of the minor axis to the major axis of an ellipsoidal pore, is commonly used to indicate pore types (Guo et al., 2015; Fournier et al., 2018; Guo et al., 2021; Wang et al., 2021, 2022). For example, stiff pores with a high aspect ratio (0.7-1.0) correspond to vuggy or moldic pores; reference pores (or matrix pores) with a moderate aspect ratio (0.1–0.25) represent interparticle or intercrystallie pores; soft pores with a lower aspect ratio (0.01-0.05) indicate cracks. Based on this concept, several studies have explored rock-physics-based methods, particularly inclusion-based effective medium theories, to characterize complex pore structures in carbonate reservoirs. For instance, Kumar and Han (2005) used the differential effective medium (DEM) to invert the average aspect ratio of different pore types based on velocities calculated using Hashin-Shtrikman bounds and time-average equation. Li and Zhang (2014) applied a DEM analytical model-based 3D rock physics template to estimate water saturation, porosity, and equivalent pore aspect ratio. Teillet et al. (2021) applied the DEM model to determine the spatial distribution of pore aspect ratio from P-wave impedance. Despite these advances, these methods only semi-quantitatively identify the dominant pore type. There is still a need for more quantitative methods to fully characterize the complex pore networks in carbonate reservoirs.

In contrast, pore-type inversion methods appear more suitable for quantifying complex pore systems. Kumar and Han (2005) proposed an iterative procedure based on the DEM model and Gassmann's equation to estimate the average pore aspect ratio and volume fraction of different pore types from the measured porosity and P-wave velocity. Following this, Xu and Payne (2009) proposed a carbonate-specific adaption of Xu-White model to estimate volume fractions of different pore types by assigning a specific pore aspect ratio for each pore type. Sun et al. (2012) used the DEM theory and Gassmann's equation to predict the volume fraction of different pore types. Zhao et al. (2013) implemented the workflow of Xu and Payne (2009) to quantitatively describe poretype distribution in carbonate reservoirs using well logs and seismic data. Subsequent studies by Wu and Chen (2014), Li et al. (2020), Mirkamali et al. (2020), Zhang et al. (2021), and Khoshdel et al. (2022) further explored pore-type quantification. However, these studies are limited to characterizing two pore types (reference pores/stiff pores or reference pores/cracks) for a single sampling point, and are conditioned only on P-wave velocity. Although the strategy proposed by Du et al. (2024) could achieve satisfactory pore-type inversion results, its reliance on a purely

calcite or dolomite mineralogy and the requirement to assign a spatially invariable pore aspect ratio for each pore shape limit its wide application. More specifically, most of these studies focus on pore-type inversion based on well logs and 2D seismic lines, with only a few studies using 3D pre-stack seismic data.

To address the aforementioned issues, a novel two-step poretype inversion strategy is developed to characterize triple pore types and their distribution in heterogeneous carbonate reservoirs by jointly utilizing P- and S-wave velocities from well logs and seismic data. This paper first employs the extended Keys-Xu model and the Gassmann-Hill equation to construct a multi-porosity model for tight carbonate reservoirs. Then, laboratory data are used to assess the effectiveness of the developed model by comparing with model predictions. Based on the developed model, a two-step pore-type inversion method is proposed and applied to field data from the Ordovician Majiagou Formation in the Ordos Basin.

#### 2. Geological settings

The Ordos Basin, the second-largest sedimentary basin in central China, is known for its substantial oil and gas reserves (Lai et al., 2019). It can be divided into six tectonic units based on its evolution features and structural framework: Yimeng Uplift, Weibei Uplift, Jinxi Flex Fold Belt, Western Margin Thrust Belt, Yinshan Slope and Tianhuan Depression (Lai et al., 2019). The study area is located in the eastern part of the Yinshan Slope, adjacent to the Jinxi Flex Fold Belt (Fig. 1(a)).

During the Ordovician period, the basin was characterized by four main formations: the Yeli, Liangjiashan, Majiagou and Fengfeng formations. The Majiagou Formation, an important gasbearing unit, is subdivided into five members (Ma 1 to Ma 5) from bottom to top (Fu et al., 2017). Members Ma 1, Ma 3, and Ma 5 are platform evaporative facies, primarily comprised of gypsumsalt rock, limestone, and dolomite. In contrast, Members Ma 2 and Ma 4 were deposited in a shallow-water carbonate platform environment, with lithologies including dolomite and lime (He et al., 2022).

The marine carbonate formations of Ma 1 and Ma 3 members act as source rocks, supplying gas source to the Ma 4 member reservoir through faults and microcracks (Wei et al., 2017). The Ma 4 member features structural-lithologic traps and several sets of limestone and gypsum-salt cap rocks in the Ma 4 and Ma 5 members, which impede the upward gas migration. These conditions make the Ma 4 member of the Ordovician Majiagou Formation a prime target for natural gas exploration.

The focus of this study is the tight carbonate reservoir within the subsalt Ma 4 member (Fig. 1(b)). This interval is characterized by intra-platform mound facies along the Mizhi Depression, with a lithology predominantly comprising finely crystalline dolomite and dolomitic limestone. Petrophysical measurements of core samples from the Ma 4 member reveal low porosity (0.34%–6.73%), low permeability (0.0002–1.46 mD), and significant heterogeneity (Fig. 2). Two distinct trends of dependence between permeability and porosity can be observed from core data. One trend is related to reference porosity present in dolostone reservoirs, and showing a proportional increase in permeability with increasing porosity. The other shows an increase in permeability even when the porosity is extremely low, indicating the presence of cracks in the limestone reservoirs.

#### 3. Rock physics modeling of carbonate reservoirs

Given the diverse mineral components, complex pore structures, and uneven fluid distribution in carbonate reservoirs, we

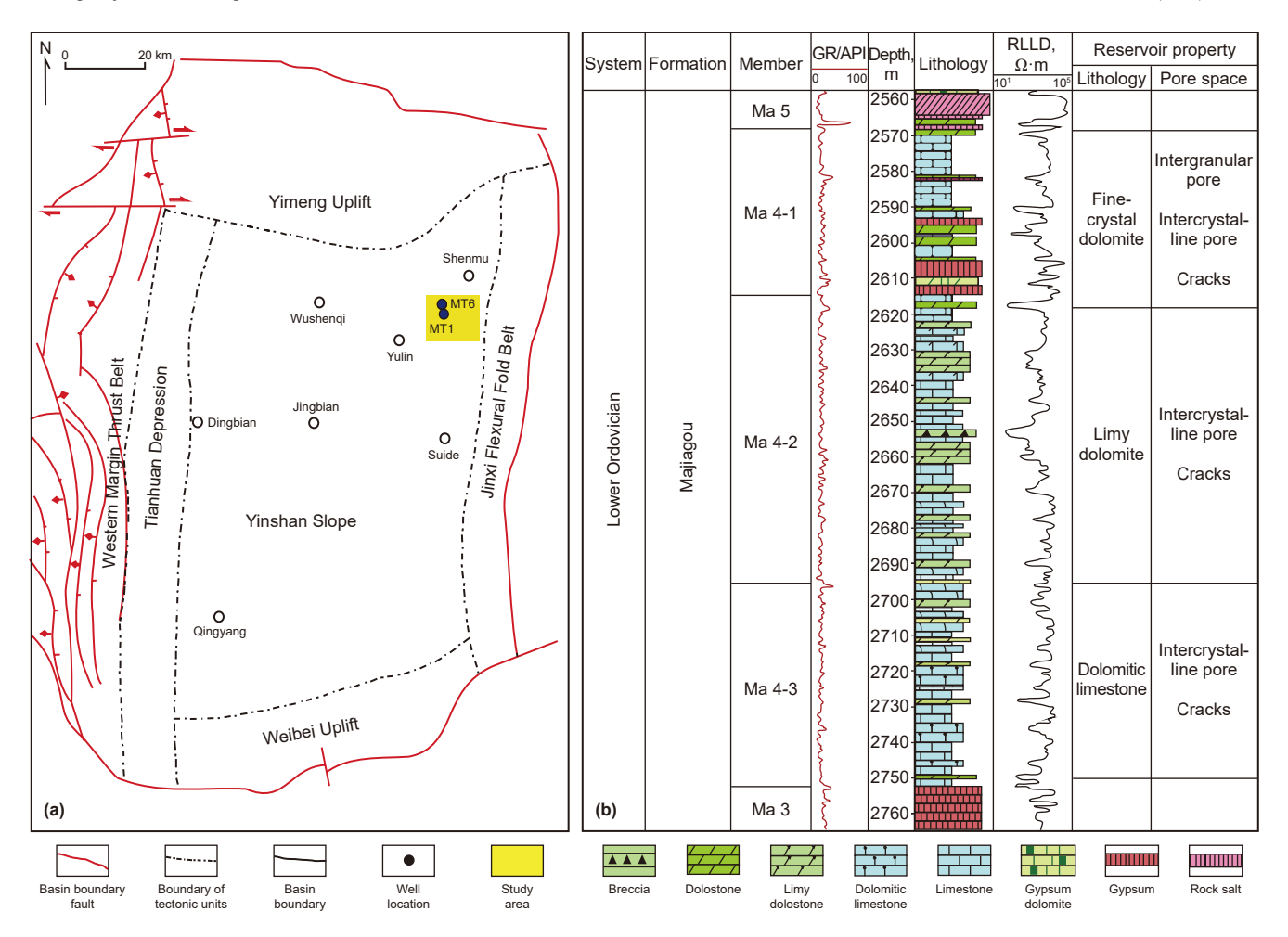
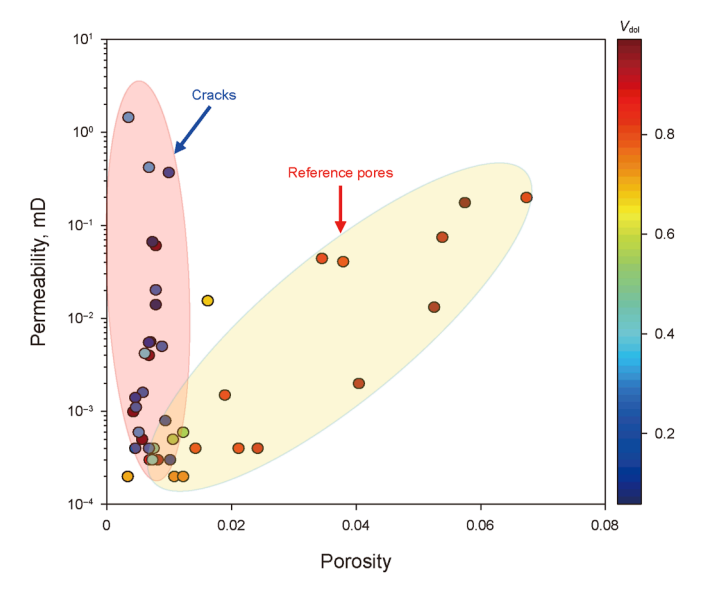


Fig. 1. (a) The tectonic units of the Ordos Basin and location of the study area; (b) stratigraphic column of the fourth member of Ordovician Majiagou Formation (modified from Fu et al. (2021)).



**Fig. 2.** The relationship between permeability and porosity for carbonate reservoirs in the Ma 4 member. The red and yellow areas indicate the rocks with cracks and reference pores, respectively.  $V_{\rm dol}$  indicates the volume fraction of dolomite.

developed a Triple-Pore Equivalent Medium (TPEM) model for tight carbonate reservoirs. This model integrates the Voigt-Reuss-Hill average, the extended Keys-Xu model, and the Gassmann-Hill equation to gradually incorporate mineral matrix, various pore types, and pore fluids. The TPEM model simplifies the complex pore structures into three effective pore types: stiff pores, reference pores, and cracks. The main steps in rock physics modeling, including calculating elastic moduli of the rock matrix, dry rock, and fluid-saturated rocks, are presented in Fig. 3.

#### 3.1. Elastic moduli of rock matrix

The carbonate reservoirs in the study area consist primarily of calcite and dolomite, with a small amount of low quartz, and clay minerals. The bulk modulus ( $K_{\rm ma}$ ) and shear modulus ( $G_{\rm ma}$ ) of the rock matrix are calculated using the Voigt-Reuss-Hill (VRH) average (Hill, 1952):

$$K_{\text{ma}} = \frac{1}{2} \left[ \sum_{i=1}^{M} f_i K_i + \left( \sum_{i=1}^{M} f_i / K_i \right)^{-1} \right],$$
 (1)

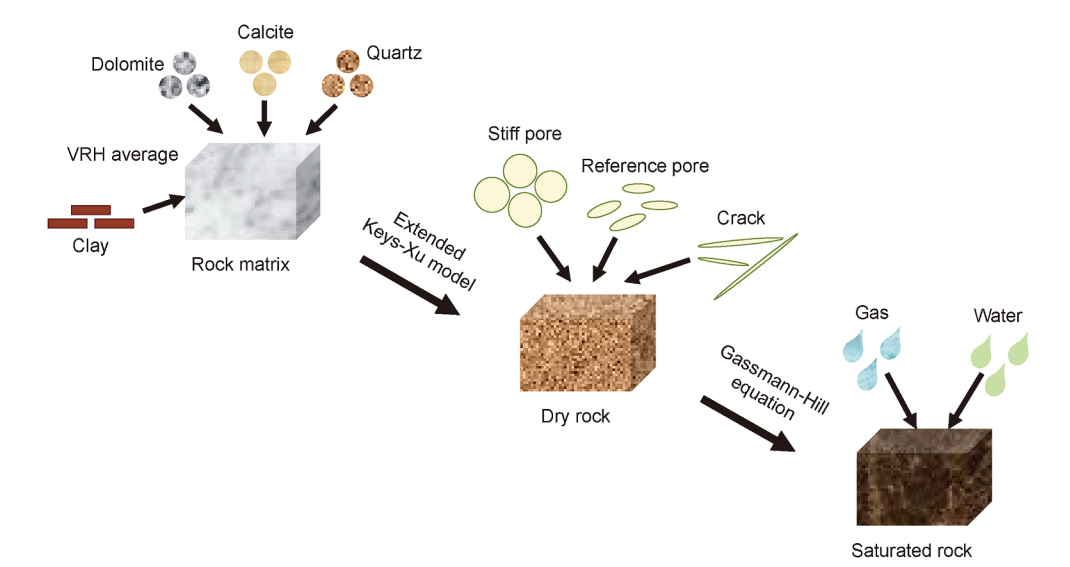


Fig. 3. Rock physics modeling for carbonate reservoirs with triple pore types.

$$G_{\text{ma}} = \frac{1}{2} \left[ \sum_{i=1}^{M} f_i G_i + \left( \sum_{i=1}^{M} f_i / G_i \right)^{-1} \right],$$
 (2)

where  $f_i$ ,  $K_i$  and  $G_i$  represent the fraction, bulk modulus, and shear modulus of the ith mineral component, respectively; and M is the total number of mineral components.

#### 3.2. Elastic moduli of dry rock

The Keys-Xu model (Keys and Xu, 2002) is commonly used to predict the elasticity of rocks. It integrates the DEM approach (Norris, 1985) with the Kuster-Toksöz (KT) equation (Kuster and Toksöz, 1974) to address the limitation associated with the sparse concentrations of pores. For carbonate reservoirs, the extended Keys-Xu model that accommodates stiff pores, reference pores, and cracks can be used to compute the bulk modulus ( $K_{\rm dry}$ ) and shear modulus ( $K_{\rm dry}$ ) of dry rock as follows:

$$K_{\text{dry}} = K_{\text{ma}} (1 - \phi)^P, \tag{3}$$

$$G_{\text{drv}} = G_{\text{ma}}(1 - \phi)^{Q}, \tag{4}$$

where  $\phi$  denotes porosity, P and Q are geometric factors related to the pore aspect ratio:

$$P = \frac{1}{3} \sum_{l=c} v_l T_{\text{iijj}}(\alpha_l), \tag{5}$$

$$Q = \frac{1}{5} \sum_{l=s,r,c} v_l \left[ T_{ijij}(\alpha_l) - \frac{1}{3} T_{iijj}(\alpha_l) \right], \tag{6}$$

where  $v_{\rm S}$ ,  $v_{\rm T}$  and  $v_{\rm C}$  represent the volume fractions of stiff pores, reference pores, and cracks, respectively; while  $\alpha_{\rm S}$ ,  $\alpha_{\rm T}$  and  $\alpha_{\rm C}$  are the aspect ratios for stiff pores, reference pores, and cracks, respectively;  $T_{\rm ijij}(\alpha_l)$  and  $T_{\rm iijj}(\alpha_l)$  are functions of the pore aspect ratio (Berryman, 1980).

#### 3.3. Elastic moduli of saturated rock

To determine the elastic moduli of fluid-saturated rocks, we use fluid substitution technology to fill the pore spaces of dry rock. The

Gassmann equation (Gassmann, 1951) is employed under the low-frequency assumption to calculate the bulk modulus ( $K_{\text{sat}}$ ) and shear modulus ( $G_{\text{sat}}$ ) of saturated rocks:

$$K_{\text{sat}} = K_{\text{ma}} \frac{\phi K_{\text{dry}} - (1 + \phi) K_{\text{fl}} K_{\text{dry}} / K_{\text{ma}} + K_{\text{fl}}}{(1 - \phi) K_{\text{fl}} + \phi K_{\text{ma}} - K_{\text{fl}} K_{\text{dry}} / K_{\text{ma}}},$$
(7)

$$G_{\text{sat}} = G_{\text{drv}} \tag{8}$$

where  $K_{fl}$  represents the bulk modulus of the pore fluid.

In tight carbonate reservoirs, where gas and water are unevenly distributed in the pore space, the Gassmann-Hill equation can be used to determine the overall saturated bulk modulus ( $\tilde{K}_{\rm sat}$ ):

$$\tilde{K}_{\text{sat}} = \left(\frac{S_{\text{w}}}{K_{\text{sat,w}} + \frac{4}{3}G_{\text{sat}}} + \frac{1 - S_{\text{w}}}{K_{\text{sat,g}} + \frac{4}{3}G_{\text{sat}}}\right)^{-1} - G_{\text{sat}}$$
(9)

where the bulk moduli of fully water-saturated ( $K_{\text{sat,w}}$ ) and gas-saturated ( $K_{\text{sat,g}}$ ) rocks are calculated using Eq. (7);  $S_{\text{w}}$  denotes the water saturation.

#### 4. Model validation with laboratory data

The quantitative relationship between P- and S-wave velocities, porosity, and pore types in tight carbonate reservoirs forms the theoretical foundation for seismic pore-type characterization. To evaluate the developed TPEM model, we conducted numerical simulations to examine how porosity and the volume fractions of different pore types affect elastic behaviors. These simulations were then compared with experimental data to refine our

 Table 1

 Elastic modulus and density of each component.

Components	Bulk modulus, GPa	Shear modulus, GPa	Density, g/cm <sup>3</sup>
Calcite	76.8	32	2.71
Dolomite	94.5	45	2.87
Clay	20.9	6.85	2.58
Quartz	38	44	2.65
Water	2.25	0	1.03
Gas	0.12	0	0.23

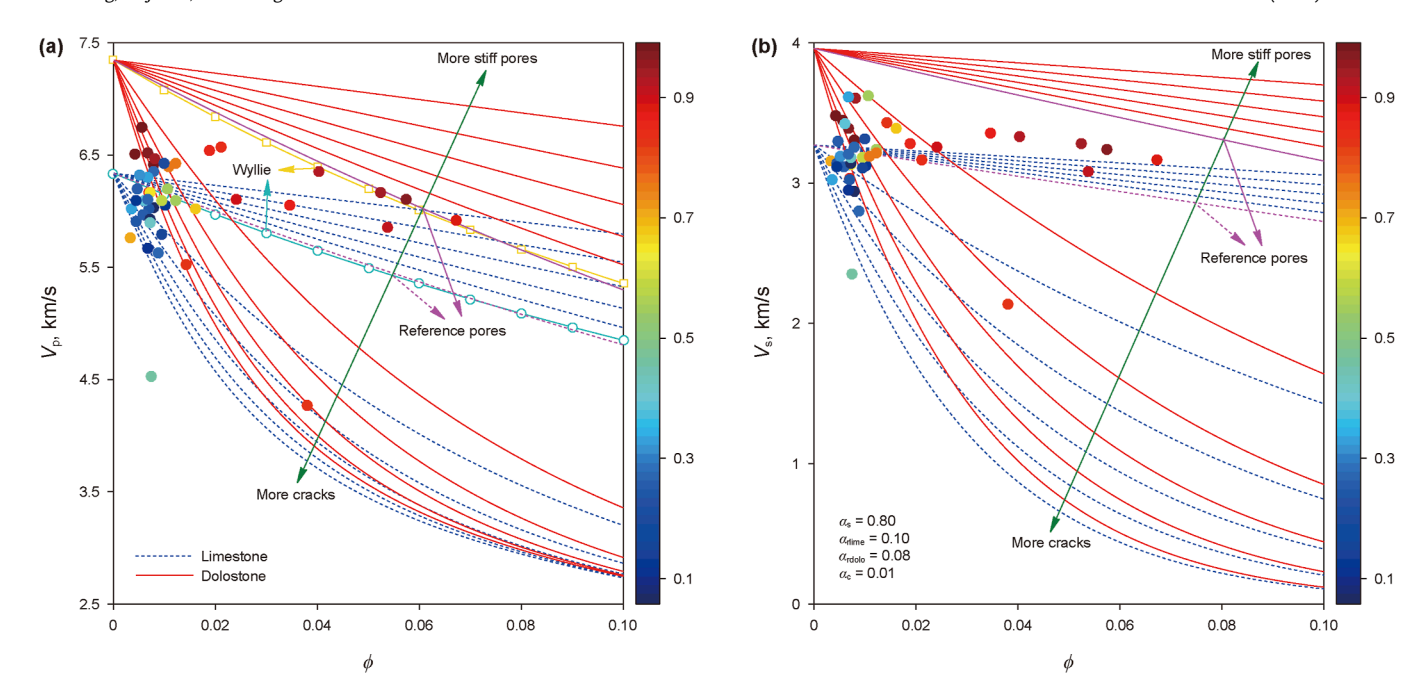


Fig. 4. Quantitative relationship among pore type, porosity, and P- (a) and S-wave (b) velocities for limestone (blue dotted lines) and dolostone (red solid lines) reservoirs.

understanding of pore aspect ratios for various pore types in the studied region. The elastic modulus and density of each rock component used in the calculations are provided in Table 1.

We evaluated the effectiveness of the TPEM model using P- and S-wave velocity measurements from 45 limy dolostone samples collected in the study area. Fig. 4 illustrates the effects of lithology, porosity, and pore type on P- and S-wave velocities in limestone and dolostone reservoirs. Following the approach of Wang et al. (2024), aspect ratios for stiff pores and cracks were set as 0.8 and 0.01, respectively. By fitting the Wyllie's time-average reference lines and TPEM model predictions (Fig. 4(a)), the aspect ratios of reference pores were determined as  $\alpha_{\text{rlime}} = 0.10$  for limestone samples and  $\alpha_{\text{rdolo}} = 0.08$  for dolostone samples. As expected, both P- and S-wave velocities decrease as porosity increases. However, the sensitivity of these velocities to porosity varies depending on the pore types. In pore systems dominated by stiff pores and reference pores, velocities decrease linearly with porosity but increase with the fraction of stiff pores. In contrast, pore systems

containing cracks and reference pores exhibit a sharp decline in velocities with increasing porosity and crack fraction. These findings suggest that cracks have a more pronounced impact on elastic properties compared to stiff pores. Although data points colorcoded by dolomite content show some scatter, most fall within the upper and lower boundaries defined by the dolostone line (stiff pores only) and the limestone line (cracks only). This scatter is attributed to variations in mineral composition, pore types, and porosity among the carbonate samples. Overall, the template analysis indicates that the dominant pore type in the target interval comprises the reference pores with a notable contribution from cracks.

The distribution of data points underscores the variations in Pand S-wave velocities as influenced by lithology, pore type, and porosity. At a given porosity, higher dolomite content is associated with increased P- and S-wave velocities. Data points with porosity greater than 2% and dolomite content exceeding 80% tend to fall below the dolostone reference line, while those with porosity less

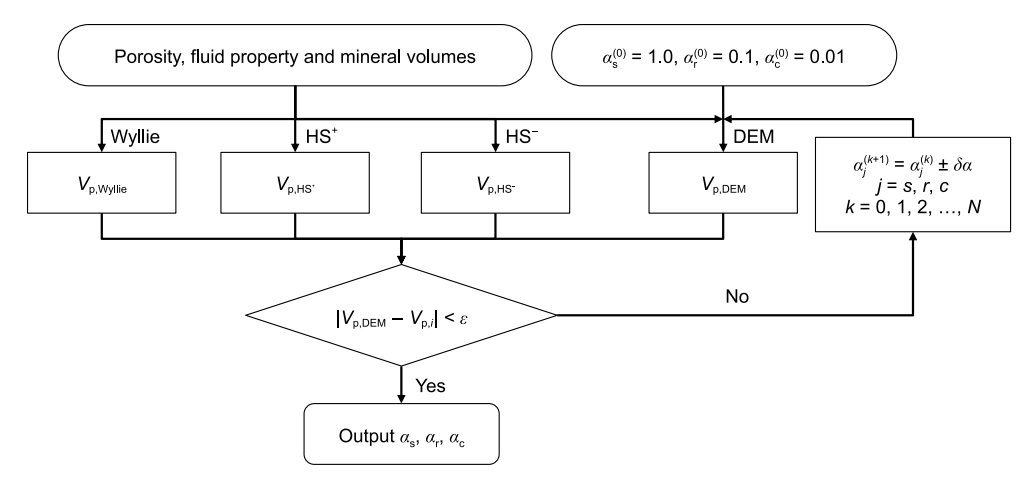


**Fig. 5.** Workflow for estimating the aspect ratios of stiff pores, reference pores and cracks.  $V_{p,i}$  (i = Wyllie, HS $^+$ , HS $^-$ ) represents the calculated P-wave velocity using Wyllie, upper and lower HS bounds, respectively.  $V_{p,DEM}$  represents the P-wave velocity calculated using the DEM model.

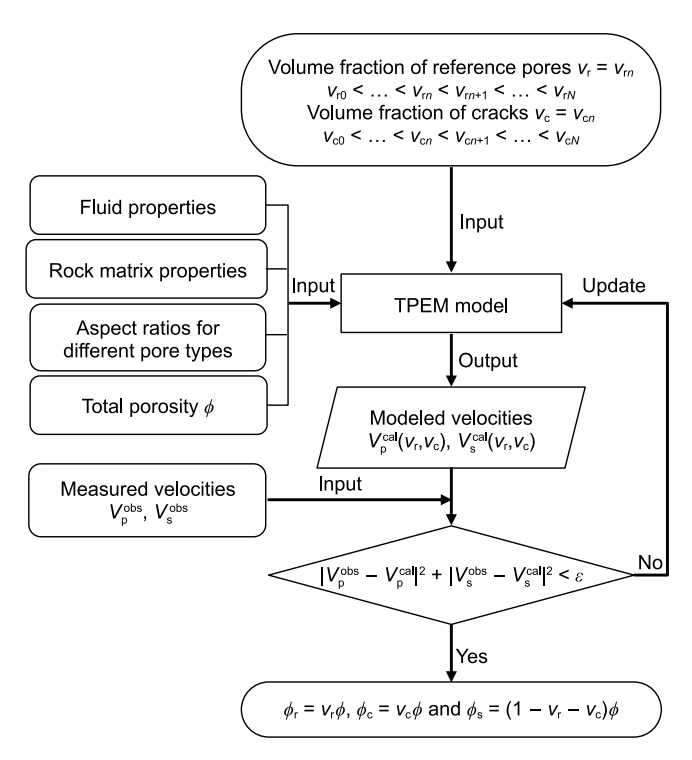
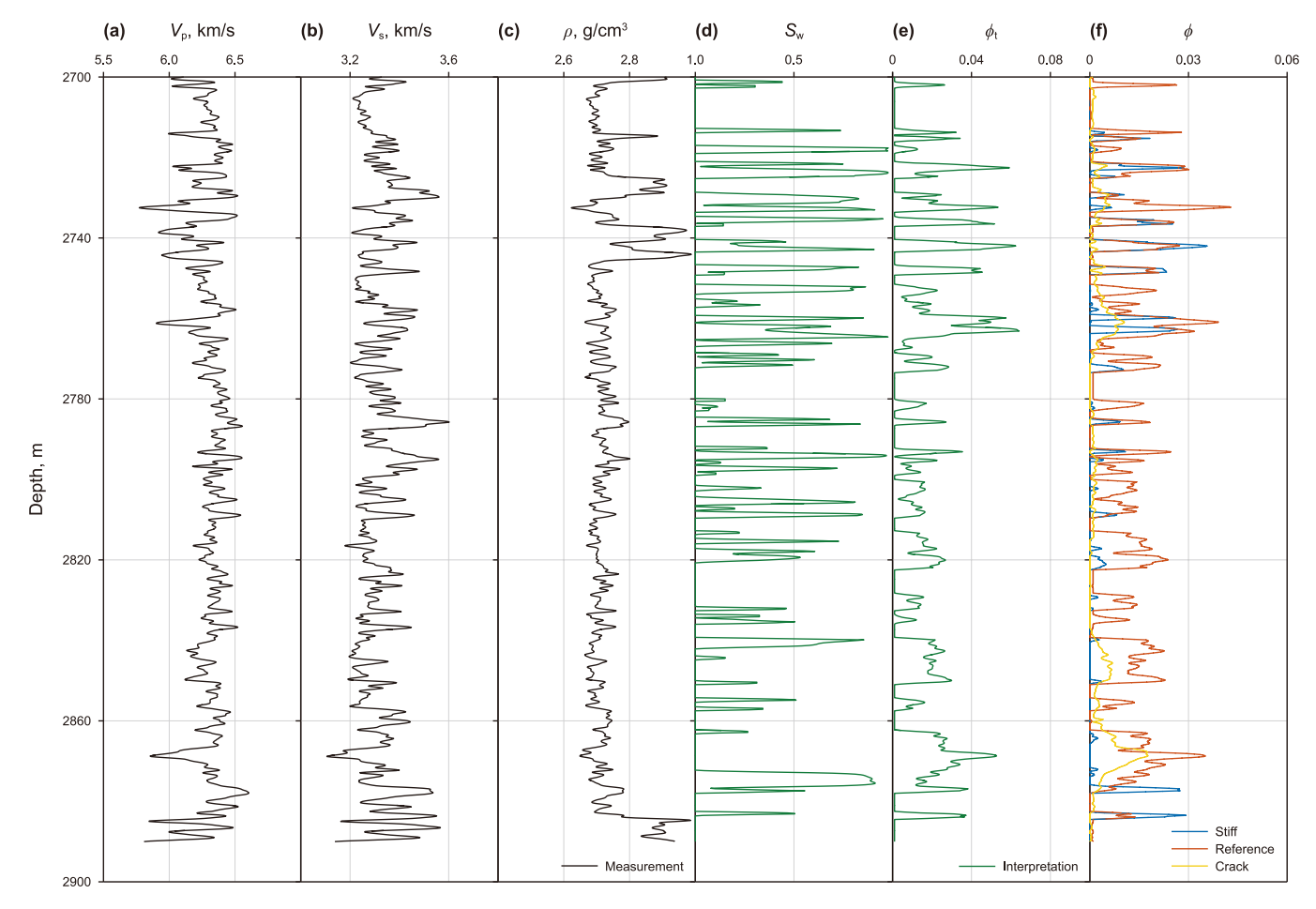


Fig. 6. Workflow for estimating the porosities of stiff pores, reference pores, and cracks.

than 2% and dolomite content below 20% cluster around the limestone reference line. This pattern suggests that limy dolomite formations are prone to develop cracks, likely caused by dissolution collapse and tectonic rupture. In contrast, dolomitic limestones exhibit more complex pore structures, including intercrystalline, intergranular, intragranular pores, and cracks, driven by differential compaction, intense dissolution, and penecontemporaneous dolomitization. These insights contribute to a deeper understanding of the pore structures in tight carbonate reservoirs within the Ma 4 member, providing a robust theoretical framework for improving pore type estimation accuracy in rock physics analyses.

#### 5. Two-step triple pore-type inversion method

In this section, we present a new two-step triple pore-type inversion (TPTI) method to predict the aspect ratio and relative volume percentage of each pore type. Unlike traditional pore-type inversion methods, our method considers three pore types, including stiff pores, reference pores, and cracks, for each sampling point, and incorporates the spatial variations in the pore aspect ratio for each pore type. Before performing pore-type quantification, it is essential to determine the pore aspect ratio for each pore type. Fig. 5 outlines the workflow for estimating pore aspect ratio of stiff pores ( $\alpha_s$ ), reference pores ( $\alpha_r$ ) and cracks ( $\alpha_c$ ). The procedure consists of four main steps: 1) set the initial aspect ratio with search ranges of [0.5, 1.0] for  $\alpha_s$ , [0.1, 0.5] for  $\alpha_r$  and [0.001, 0.1] for  $\alpha_c$ ; 2) calculate the P-wave velocities of carbonate rocks with



**Fig. 7.** Logging data and interpretation results of well MT 6. From left to right, the panels display P-wave velocity, S-wave velocity, density, water saturation, total porosity, and porosities for different pore types. The blue, red and yellow lines represent the stiff pores  $(\phi_s)$ , reference pores  $(\phi_r)$ , and cracks  $(\phi_c)$  respectively.

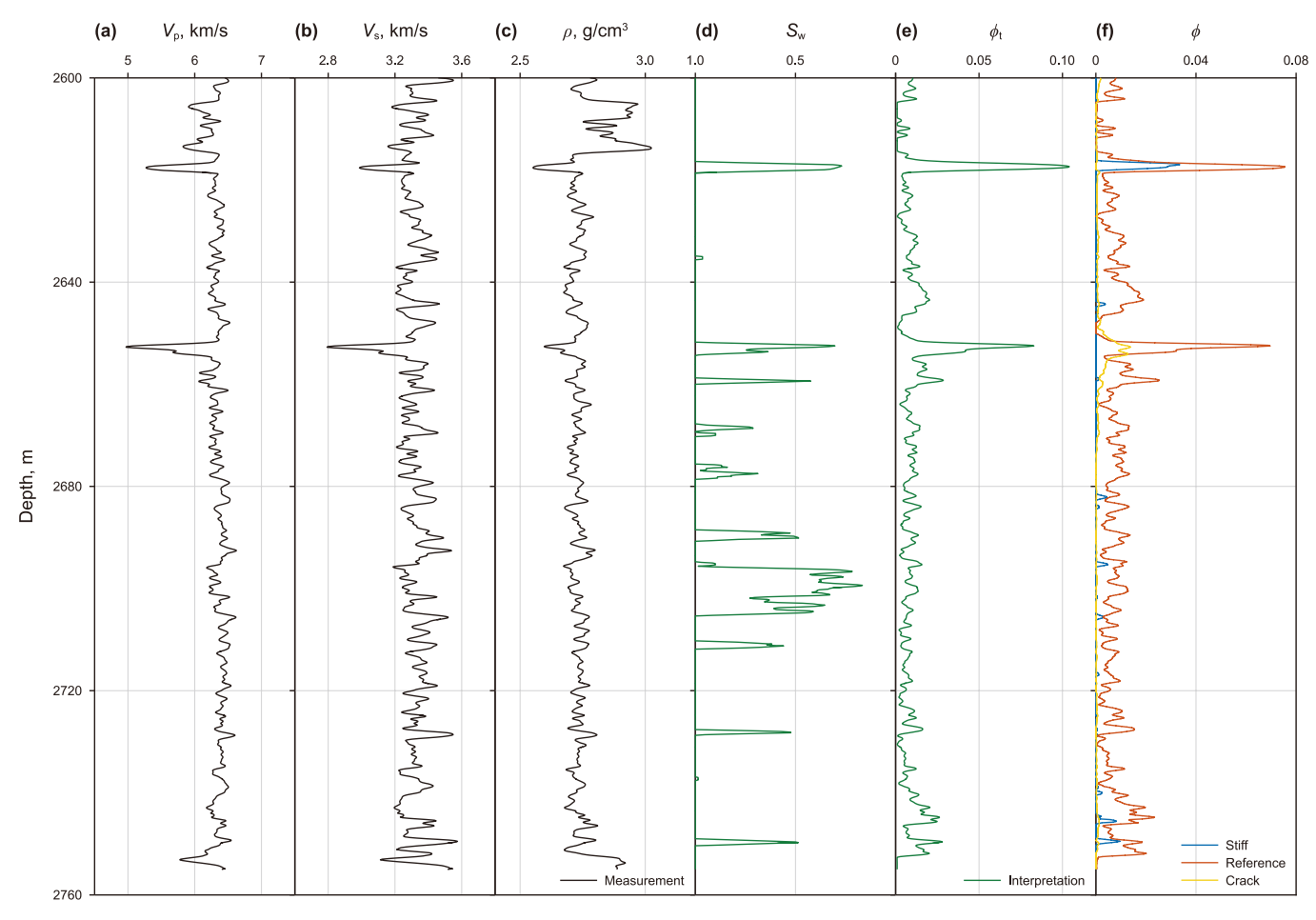


Fig. 8. Logging data and interpretation results of well MT 1. From left to right, the panels display P-wave velocity, S-wave velocity, density, water saturation, total porosity, and porosities for different pore types. The blue, red and yellow lines represent the stiff pores, reference pores, and cracks, respectively.

stiff pores ( $V_{\rm p,HS^+}$ ), cracks ( $V_{\rm p,HS^-}$ ), and reference pores ( $V_{\rm p,Wyllie}$ ) using the upper and lower Hashin-Shtrikman (HS) bounds and Wyllie's time-average equation, respectively; 3) iteratively apply the DEM model by assigning an initial aspect ratio to estimate the P-wave velocity of rocks with different pore types; 4) determine the pore aspect ratio for each pore type by minimizing the mismatch between the DEM-based velocity and the velocities predicted by the HS bounds and Wyllie's equation.

Fig. 6 shows the workflow for determining the porosity of each pore type from P- and S-wave velocities based on the TPEM model. Here, the water saturation, total porosity, and volumetric fractions of mineral components can be obtained from conventional well logs to constrain the pore-type inversion. The P- and S-wave velocities are then computed with the total porosity, the fluid and mineral properties, as well as the estimated aspect ratios for all pores for the preset value range of volumetric fractions of reference pores ( $\nu_{\rm r}$ ) and cracks ( $\nu_{\rm c}$ ). Given the measured and inverted P- and S-wave velocities, the percentages of different pore types can be obtained by solving a nonlinear problem for minimization of cost function:

$$J(\nu_{\rm r}, \nu_{\rm c}) = \min \left[ \left( V_{\rm p}^{\rm cal}(\nu_{\rm r}, \nu_{\rm c}) - V_{\rm p}^{\rm obs} \right)^2 + \left( V_{\rm s}^{\rm cal}(\nu_{\rm r}, \nu_{\rm c}) - V_{\rm s}^{\rm obs} \right)^2 \right]$$
(10)

where  $V_{\rm p}^{\rm obs}$  and  $V_{\rm s}^{\rm obs}$  are the observed P- and S-wave velocities, respectively;  $V_{\rm p}^{\rm cal}$  and  $V_{\rm s}^{\rm cal}$  are the calculated P- and S-wave velocities, respectively.

Based on Eq. (10), an enumeration method, grid searching algorithm, is used to find an optimal solution. After determining the fractions of reference pores and cracks, the percentage of stiff pores can be obtained as the sum of the volume percentages of all pore types is equivalent to one. Finally, the porosities of stiff pores  $(\phi_s)$ , reference pores  $(\phi_r)$ , and cracks  $(\phi_c)$  can be calculated by multiplying their corresponding fractions with total porosity.

This workflow is particularly suitable for interpreting ultrasonic observations and well logging data when quantifying pore types. However, to adapt this method for seismic data, the effects of fluid content and mineralogy should be calibrated locally with laboratory data and logging measurements. Previous studies suggest that the pore-type inversion results are little influenced by variations in water saturation, especially for total porosity lower than 10% (Teillet et al., 2021; Du et al., 2024). In the studied intervals, the total porosity ranges from 0% to 10%. In this regard, it is plausible to use the distribution of water saturation derived from the horizon-guided well-log interpolation as input. For mineralogy effects, the elastic moduli of rock matrix can be determined using a velocity-porosity template based on well-log data from the study area.

Following the outlined workflow, we can infer the porosities of different pore types from seismic data. The inversion procedure begins with estimating P- and S-wave velocities and density via prestack seismic inversion. Subsequently, the total porosity is derived from the inverted density volume. The spatially varying pore aspect ratio for each pore type is then obtained using the inversion workflow outlined in Fig. 5. Next, the pore-type quantification is performed using the proposed TPTI approach, with the extracted P-

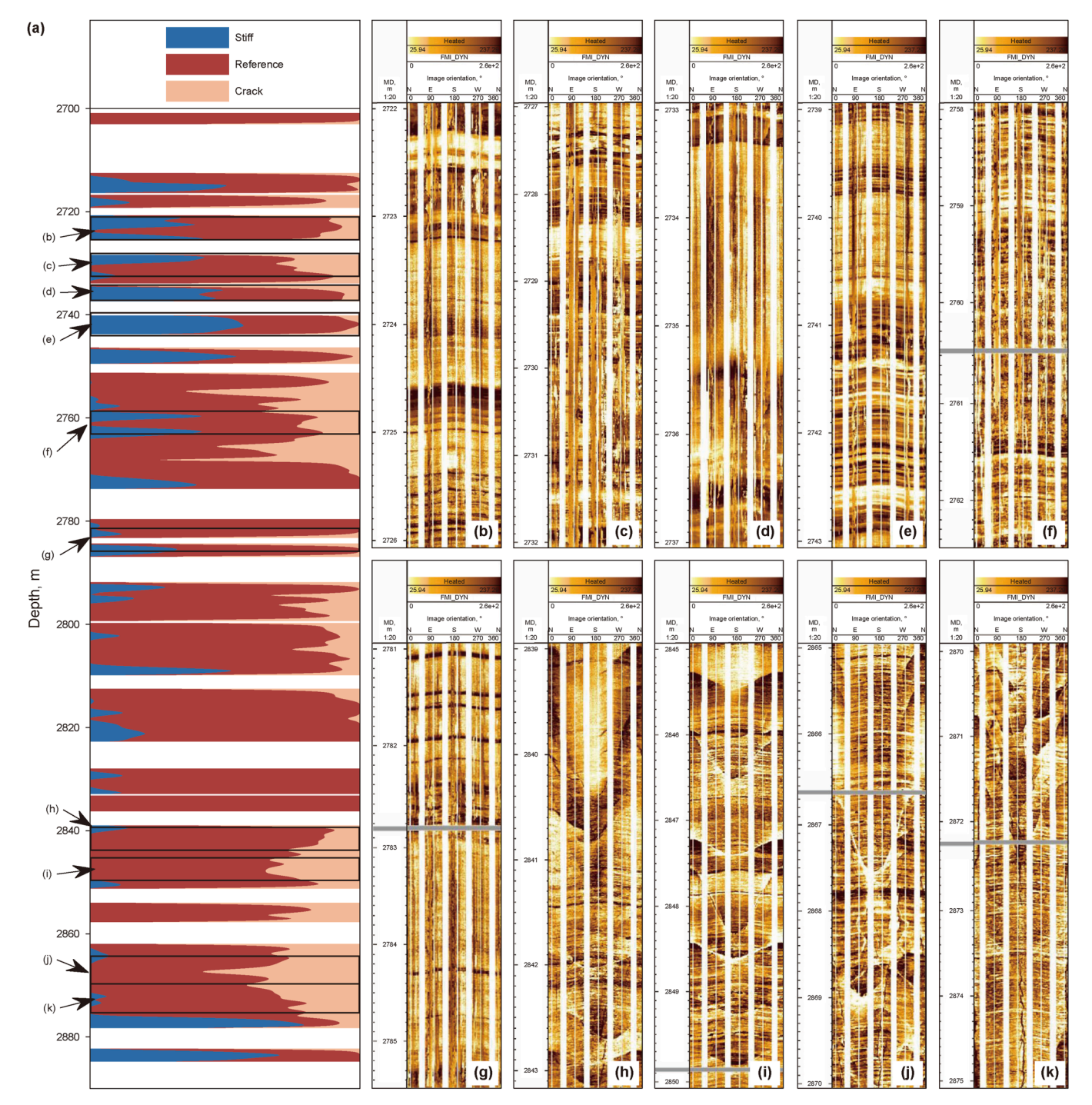


Fig. 9. Comparison between the pore-type interpretation results and pore types indicated from FMI logs for well MT 6. (a) The area of blue, red, and pink represent volume fraction of stiff pores, reference pores, and cracks, respectively; (b)-(k) FMI logs for different intervals.

and S-wave velocities and total porosity as inputs. Finally, the distribution of different pore types are determined, which can be used to assess the quality of tight carbonate reservoirs.

#### 6. Real application

We evaluate the two-step TPTI method by assessing its pore type estimation results using two sets of well-log data and elastic attributes inverted from a 3D pre-stack seismic cube. First, acoustic, resistivity, and density logs from two wells were used to interpret reference porosity, crack porosity, and total porosity,

respectively. These estimates, validated through Formation Micro-Imager (FMI) logs, were then employed to examine the performance of the proposed TPTI method. Finally, the pre-stack seismic inversion results, including density, P- and S-wave velocities, were used to quantify the spatial distribution of pore structures in carbonate reservoirs of the Ordos Basin, China.

#### 6.1. Well-log data test

We first tested the proposed two-step TPTI method with spatially-varying pore aspect ratio using well-log data from two

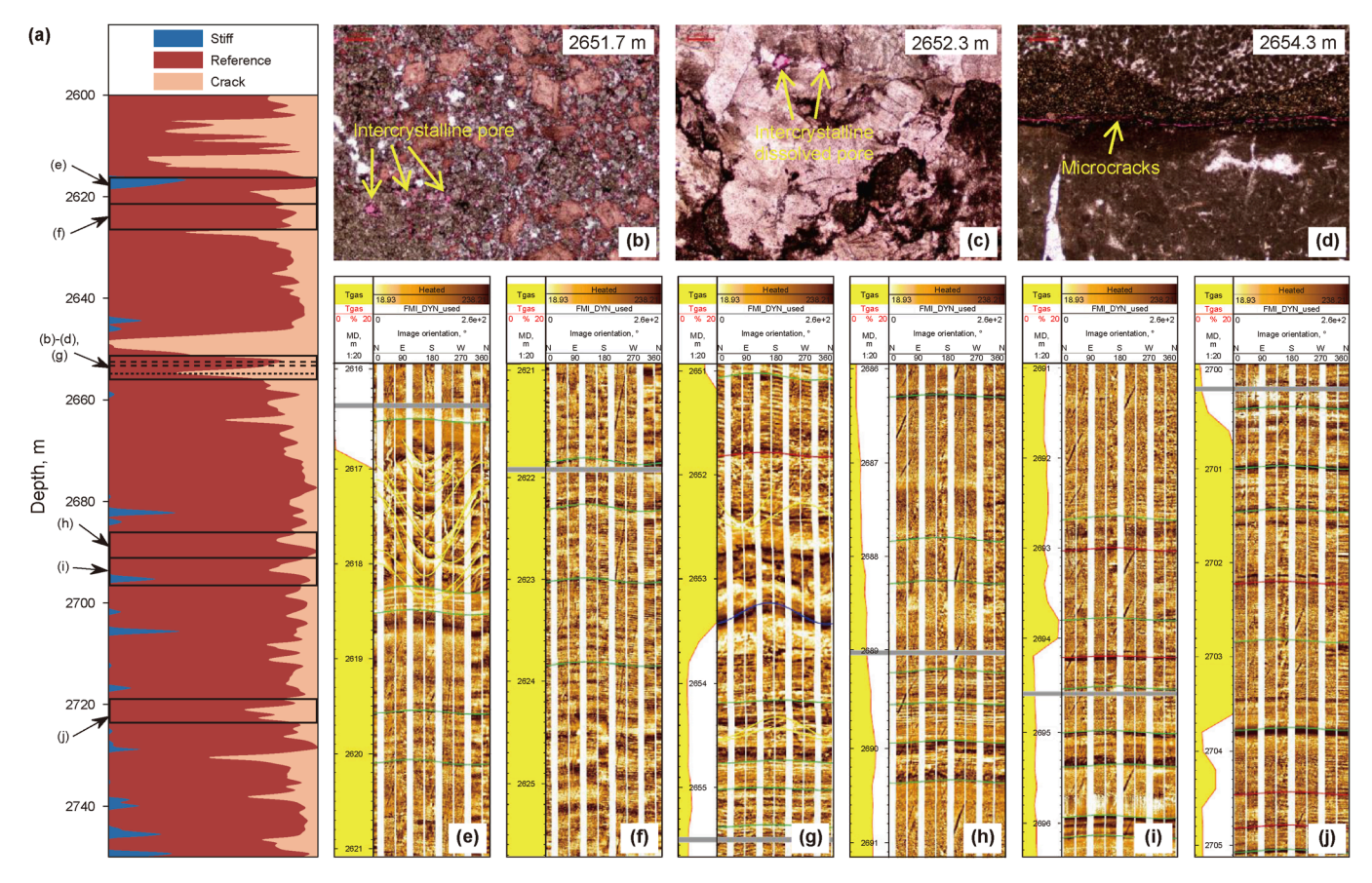


Fig. 10. Comparison between the pore-type interpretation results and pore types indicated from thin sections and FMI logs for well MT 1. (a) The area of blue, red, and pink represent volume fraction of stiff pores, reference pores, and cracks, respectively; (b)–(d) thin sections for different core samples with their depths in meter; (e)–(j) FMI logs for different intervals.

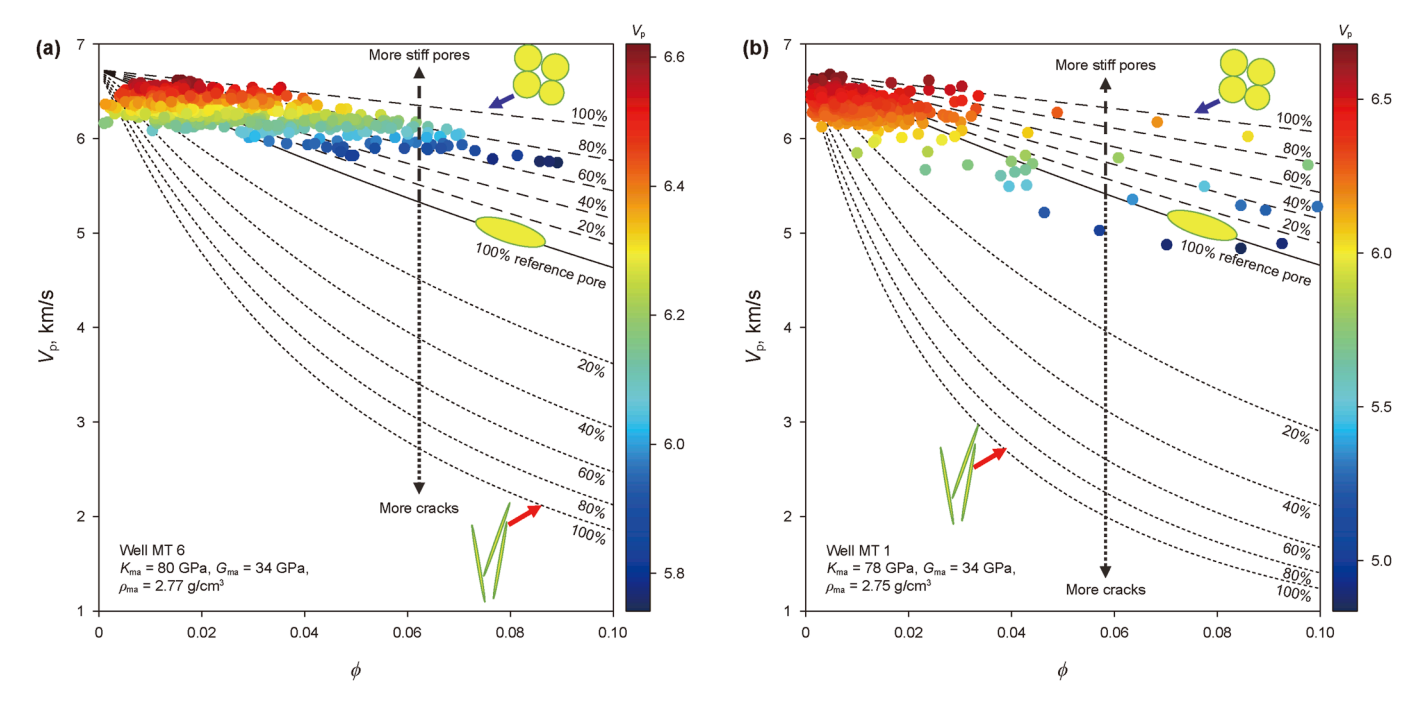


Fig. 11. Determination of the elastic moduli of rock matrix with the velocity-porosity template using well-log data: (a) Well MT 6; (b) Well MT 1.

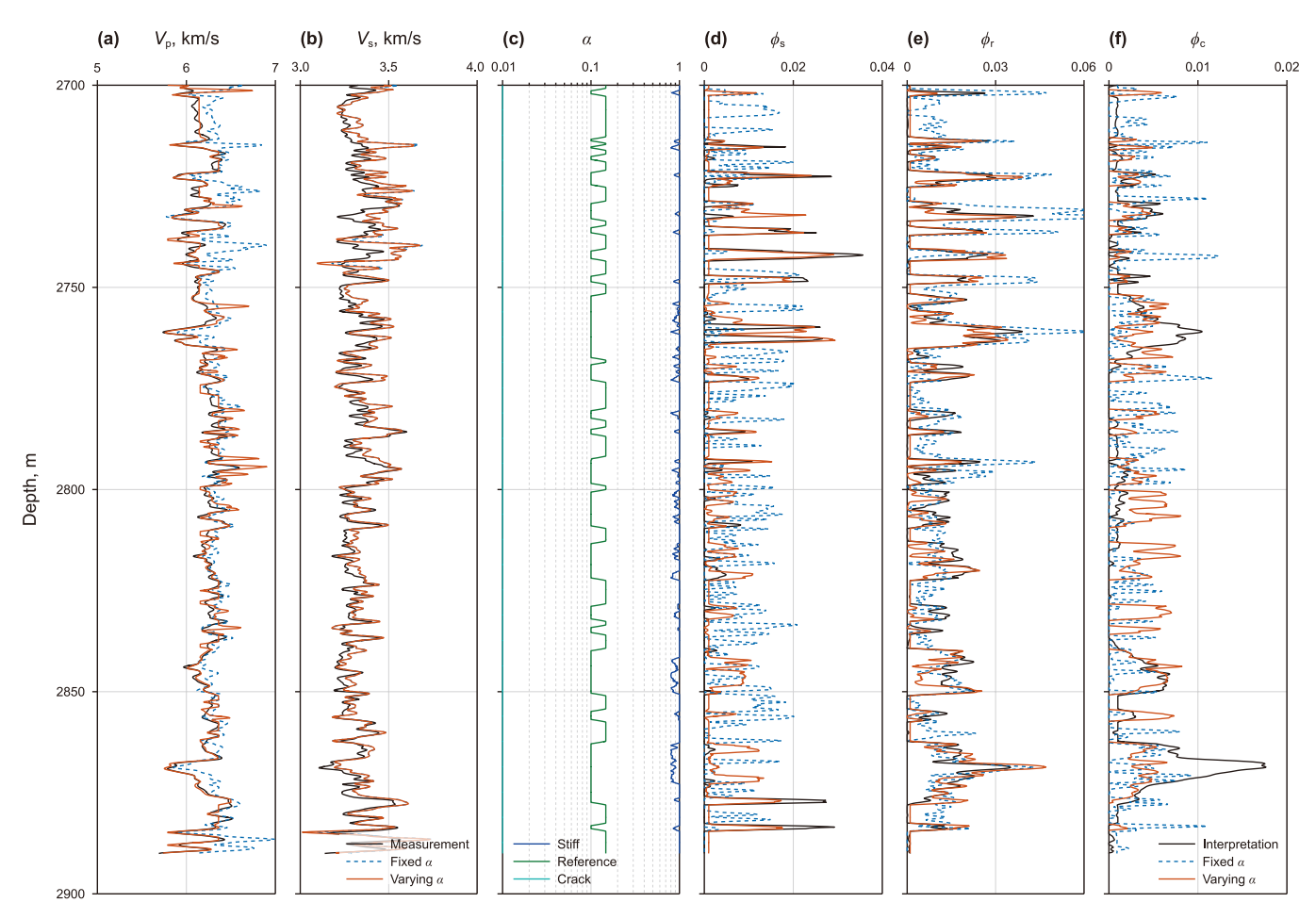


Fig. 12. Inversion results of pore types in well MT 6: (a) P-wave velocity; (b) S-wave velocity; (c) pore aspect ratios for stiff pores, reference pores, and cracks; (d) stiff porosity; (e) reference porosity; (f) crack porosity. The solid red and dotted blue lines represent the model estimations, and black lines represent the logging measurements or interpretation results.

wells in the target area. Figs. 7 and 8 display the logging measurements and pore type interpretation results for wells MT 6 and MT 1, respectively. For well MT 6, the target interval is 2700–2890 m, with a thickness of approximately 190 m. The porosity ranges from 0% to 8.0%, and water saturation varies from 0% to 100%. For well MT 1, the target interval is 2600~2750 m, with a thickness of approximately 150 m. The porosity ranges from 0% to 11%, and water saturation varies from 25% to 100%. Following the work of Du et al. (2024), the porosities of stiff pores, reference pores, and cracks can be evaluated from density, acoustic velocity, and resistivity logs, respectively.

To verify the reliability of the pore-type interpretation results, we converted the estimated porosities (Figs. 7(f) and 8(f)) into corresponding volume fractions. Fig. 9 compares these volume fractions with FMI logs for well MT 6. The results indicate that reference pores are well-developed in the Ma 4 member, followed by stiff pores and cracks. This finding is supported by the FMI logs. For example, dark blotches in the FMI logs (Fig. 9(b)–(d)) at depths of 2712–2749 m and 2875–2885 m suggest well-developed stiff pores in these intervals. The interpretation results also indicate a high proportion of cracks between 2840 and 2880 m, consistent with the sine- or cosine-shaped curves seen in the FMI logs for intervals 2751–2770 m and 2840–2875 m (Fig. 9(f)–(k)).

In well MT 1, unlike well MT 6, the pore space is dominated by reference pores with a few cracks in the Ma 4 member as shown in Fig. 10. Stiff pores are less present in this interval. The interpretation results are confirmed by the presence of cracks and stiff pores

observed in both thin sections and FMI logs. Specially, cracks can be seen in the thin section and FMI logs at depths of 2600–2656 m, which aligns well with the interpretation results, indicating that reference pores and cracks coexist in the pore space.

To evaluate the feasibility of the inversion procedure outlined in Fig. 6, we compared the interpretation results with our inversion results. Prior to the pore-type quantification, we determined the bulk and shear moduli of the rock matrix by comparing the Pwave velocity-porosity template with well-log data from two wells, as shown in Fig. 11. Here, the aspect ratios of stiff pores, reference pores, and cracks were set to 0.8, 0.1 and 0.01, respectively. Figs. 12 and 13 compare the porosities of stiff pores, reference pores, and cracks in wells MT 6 and MT 1. These porosities were estimated from P- and S-wave velocities and total porosity data using the method with fixed aspect ratios and the proposed two-step TPTI method with varying pore aspect ratios. As shown in Figs. 12(a)-(b) and 13(a)-(b), the P- and S-wave velocities calculated using both methods closely match the measured data. Figs. 12(c) and 13(c) display the inverted pore aspect ratios of different pore types in wells MT 6 and MT 1, respectively. The estimated aspect ratio for each pore type reveal the spatial variation in pore geometry, especially for stiff pores, indicating the necessity of determining the spatially-varying pore aspect ratios before quantifying the volume fractions of different pore types.

Fig. 12(d)–(f) shows that the reference porosity estimate using the proposed method with varying aspect ratios aligns more closely with the interpretation result compared to those from the

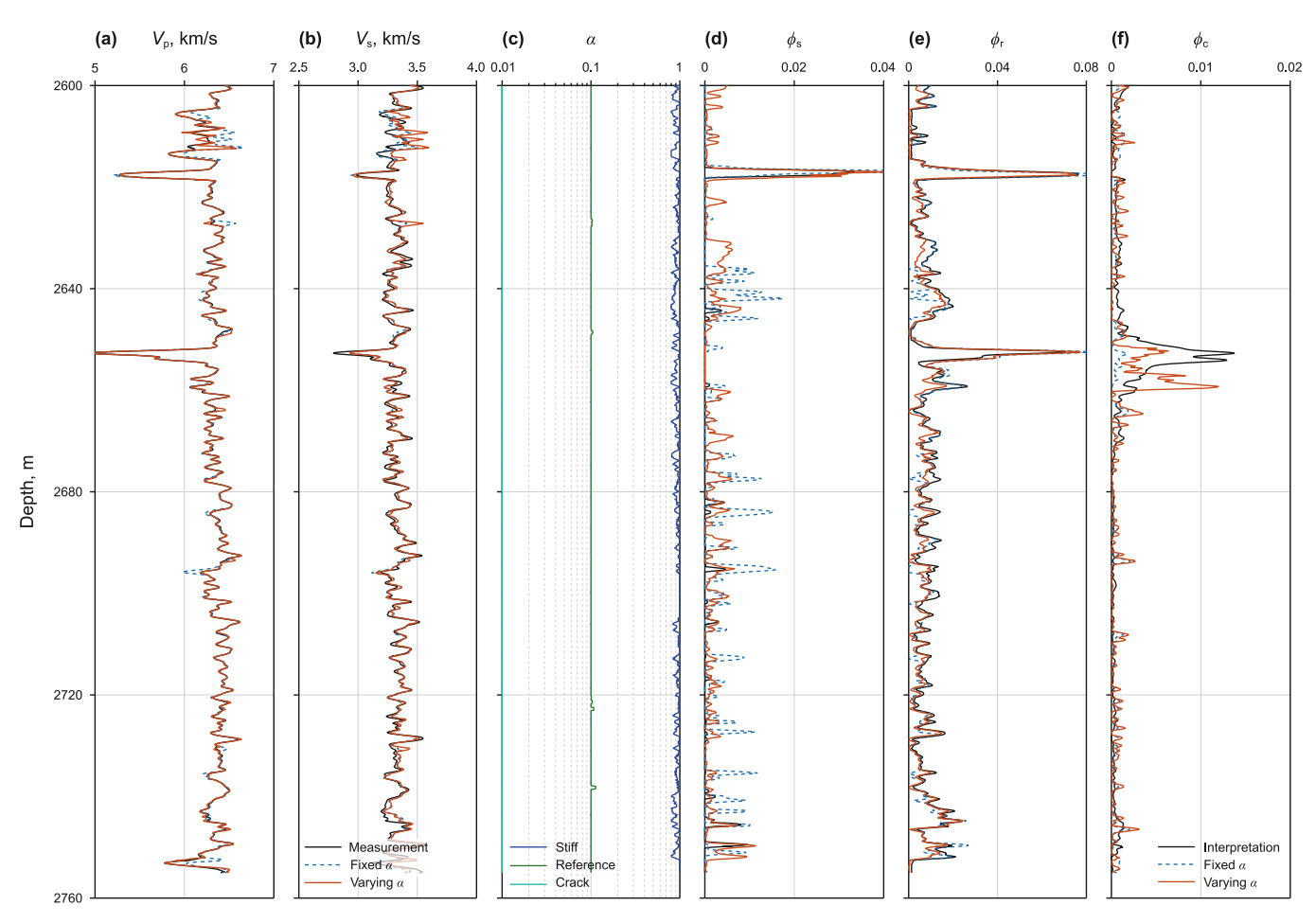


**Fig. 13.** Inversion results of pore types in well MT 1: (a) P-wave velocity; (b) S-wave velocity; (c) pore aspect ratios for stiff pores, reference pores, and cracks; (d) stiff porosity; (e) reference porosity; (f) crack porosity. The solid red and dotted blue lines represent the model estimates, while black lines represent the logging measurements or interpretation results.

TPTI method with fixed pore aspect ratios. Discrepancies in the estimates of stiff and crack porosities for intervals between 2780 m and 2880 m (Fig. 12(c)–(e)), still exhibit good consistency with the interpretation results. For well MT 6, these differences are more likely caused by the inclined well trajectory. For well MT 1, the estimated porosities for reference pores and cracks using our method show better agreement with the log-based references than the constant aspect ratio method. However, stiff porosity appears locally high (Fig. 13(c)–(e)). Overall, the porosity estimates are more consistent with the logging interpretation results. The remaining discrepancies may be attributed to the quality of well-log data, measurement errors, the applicability of the theoretical model, anisotropy induced by fractures, and reservoir heterogeneity.

#### 6.2. Seismic data application

The proposed method is further applied to a field seismic data. The 3D seismic data used in this study was acquired from the Gaojiapu area, covering approximately 200 km² in the central and eastern Ordos Basin. The dataset comprises 891 crosslines and 1191 inlines with two production wells: MT 6 and MT 1. The central frequency of this seismic data averages 35 Hz, and the sampling interval is 2 ms. Elastic parameters, such as P- and S-wave velocities and density, were extracted from seismic angle gathers by pre-stack AVO inversion techniques.

To evaluate the feasibility of the proposed TPTI method, a 2D seismic profile passing through wells MT 6 and MT 1 was analyzed. Fig. 14 displays the elastic attributes obtained from pre-stack seismic inversion. These attributes are used as input data for the pore-type inversion. Note that the angle gathers were processed to preserve amplitude, and the low-frequency initial model was interpolated from the logging data of wells MT 6 and MT 1, subject to horizon constraints. The gas-bearing intervals with the lower P-wave velocity and density around two wells suggest that pre-stack seismic inversion effectively characterizes the subsurface elastic properties.

Before proceeding with seismic pore-type estimation, it is essential to initialize the input parameters, including mineralogical content, pore aspect ratios, and fluid saturation. Due to the insufficient data, we do not attempt to quantify the volume fraction of different mineralogical composition. Instead, we determine the elastic moduli of the rock matrix based on well-log data. As shown in Fig. 11, the bulk modulus, shear modulus, and density of the rock matrix are set as 79 GPa, 34 GPa and 2.76 g/cm³, respectively. The pore aspect ratios of different pore types are treated as internal variables which can be inverted using the workflow as illustrated in Fig. 5. Following the two-step TPTI strategy, the low-frequency model of water saturation for this inversion is interpolated using well-log data from wells MT 6 and MT 1 with constraints from the seismic horizons.

Fig. 15 displays the profiles of stiff porosity, reference porosity, and crack porosity estimated from the seismic elastic properties.

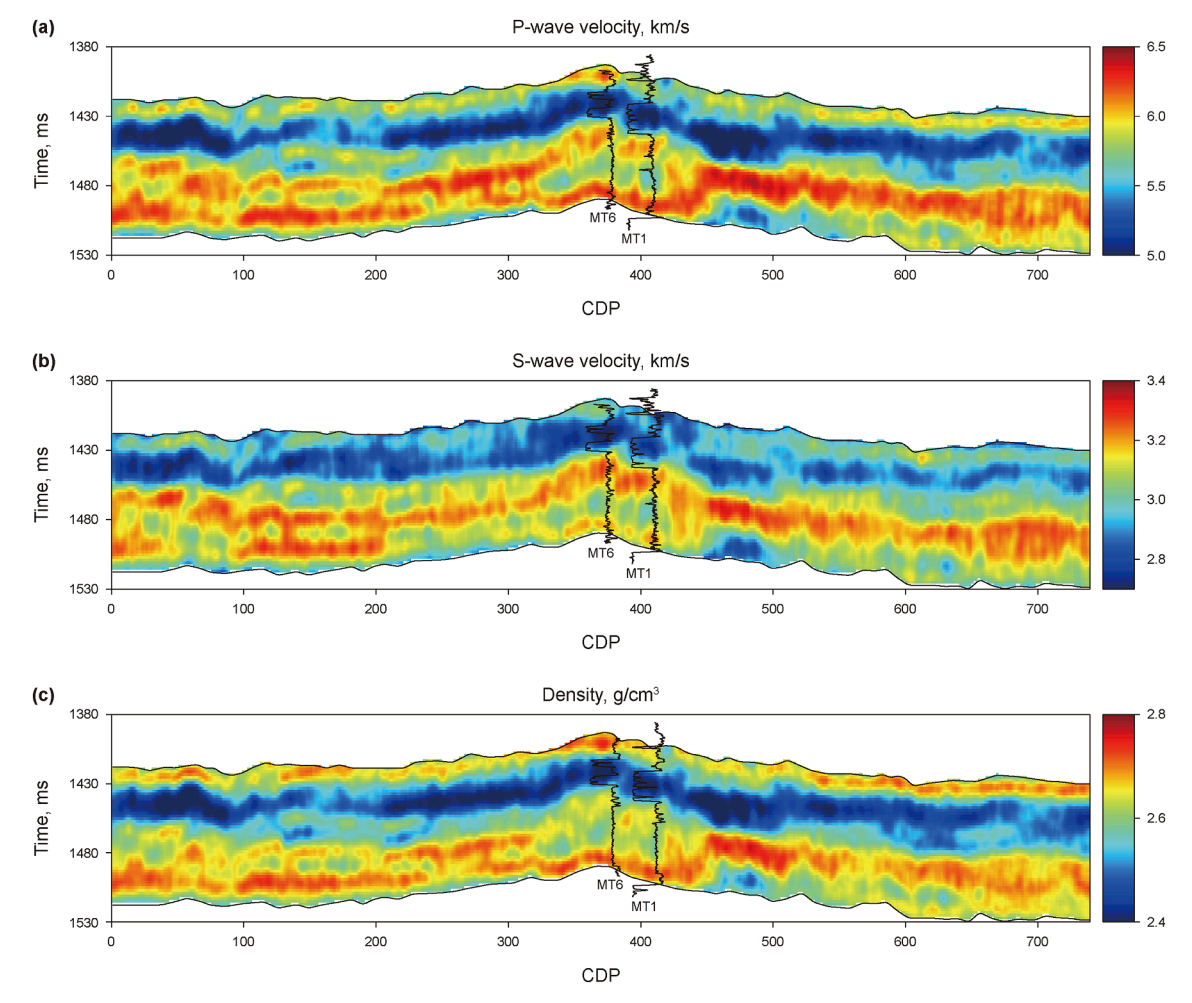


Fig. 14. AVO inversion results along the seismic lines through wells MT 6 and MT 1: (a) P-wave velocity; (b) S-wave velocity; (c) density.

Around well MT 6, reference pores and cracks are relatively well-developed, while stiff pores are less common. In contrast, near well MT 1, in addition to the presence of reference pores, a substantial number of cracks are formed, while stiff pores remain underdeveloped. This pattern may be due to the gas-bearing nature of the target interval at well MT 1, where local tectonic process, differential compaction, and excessive fluid pressure facilitate crack formation. The small number of stiff pores around well MT 6 may be attributed to extensive dissolution. These inversion results indicate that reference pores are the primary storage spaces, with cracks significantly enhancing pore connectivity and storage capacity, thereby improving reservoir quality. This geological process contributes to the formation of industrial gas fields at wells MT 1 and MT 6.

To further characterize the spatial distribution of pore types away from wells, this method was applied to 3D seismic data. Fig. 16(a)–(d) present the estimated 3D cubes of total porosity, stiff porosity, reference porosity, and crack porosity. It shows that reference pores and cracks are well-developed around wells MT 6 and MT 1, both located at local uplift and faulted zones, favoring gas accumulation and migration. This finding aligns with actual production data, which report daily gas production of  $12.2\times10^4~\text{m}^3$  from well MT 6 and  $35.24\times10^4~\text{m}^3$  from well MT 1. The pore-type inversion proves effective in identifying favorable reservoirs.

#### 7. Discussion

Accurate pore-type characterization requires a reliable rock physics relationship. To address this, we developed a new TPEM model based on the extended Keys-Xu model and the Gassmann-Hill equation. This model considers the complex pore structures, variable mineralogical composition, and uneven fluid distribution in tight carbonate reservoirs. However, it ignores the anisotropy caused by mesoscale fractures and velocity dispersion due to the wave-induced fluid flow. Models, such as the linear slip model (Chichinina et al., 2009; Chen and Innanen, 2018) and Chapman model (Chapman, 2003; Guo et al., 2016) allow for the study of anisotropic viscoelasticity in carbonate rocks with multiscale fractures. Therefore, establishing an anisotropic poroelasticity model is essential to enhance confidence in characterizing the complex pore structures of fractured porous carbonate reservoirs.

A comprehensive understanding of pore network architectures is crucial for accurately characterizing carbonate reservoirs. Based on the developed TPEM model, we propose a two-step TPTI method with varying pore aspect ratios. Unlike the dual pore-type inversion algorithm proposed by Kumar and Han (2005), our approach accounts for the coexistence of stiff pores, reference pores, and cracks at each sampling point. This enhances its reliability in capturing the complex pore structures of carbonate reservoirs. Additionally, the proposed method incorporates the

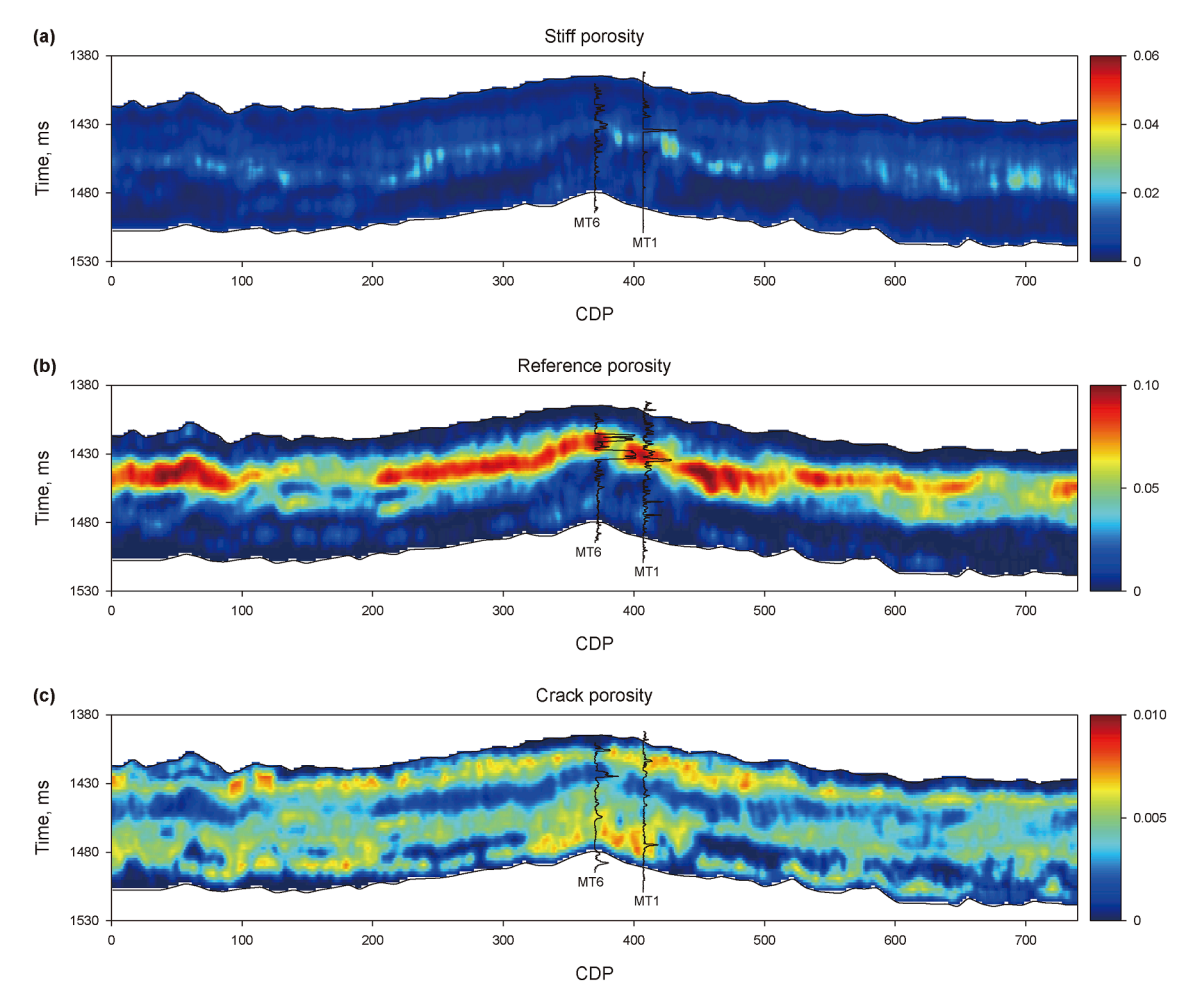


Fig. 15. Seismic inversion results for triple pore types. (a) Stiff porosity; (b) reference porosity; (c) crack porosity.

spatial variation of pore aspect ratios for each pore type, significantly improving the accuracy of pore-type inversion results, as shown in Figs. 12 and 13. The method also utilizes S-wave velocity to reduce the uncertainties in pore-type quantification. Furthermore, a global optimization algorithm instead of the traditional iterative least square approach is employed to determine the optimal combination of pore types.

Despite the good performance of the proposed method in determining the porosities of different pore types, its application is limited by the simplifications and assumptions we made. For example, this method can handle up to three pore types. Considering more pore types might improve the applicability of this method in characterizing extremely complex pore systems, but it would introduce additional parameters, increasing the uncertainty and multiplicity of the inversion results. Also, the pore aspect ratios for different pore types are estimated solely from P-wave velocity because Wyllie's time-average equation is not applicable to S-wave velocity. In practice, different pore geometries affect Pand S-wave velocities differently, resulting slight variations between the aspect ratios each other (Fournier et al., 2018). To address this discrepancy, aspect ratios obtained from P-wave and S-wave velocities can be weighted by their volume fractions (Mirkamali et al., 2020). For simplicity, we predefined the mineral proportions as constant during the pore-type inversion procedure. This approach reduces the number of unknown parameters and allows a focused analysis of pore-type inversion. However, in actual carbonate rocks, mineralogical composition is highly

complex and varies significantly with depth and region. Given that the non-reservoir intervals are almost 100% water-saturated and the reservoir intervals have high gas saturations (Figs. 7(d) and 8 (d)), water saturation may not significantly impact the inversion results, as reported by Teillet et al. (2021) and Du et al. (2024). As a result, the background model of water saturation was created through well-log data interpolation. It should be pointed out that the total porosity is calculated using the seismic-derived density. Hence, the precision of pre-stack seismic inversion will also affect the pore-type estimation. In addition to the aforementioned challenges, additional factors such as seismic data quality, the rationality of rock physics models, and the choice of inversion methodology may also influence the of pore-type inversion results. To enhance the reliability of these estimates, further research should integrate multiple physical properties, such as wave velocity and attenuation, to simultaneously characterize spatial variations of pore geometries and reservoir properties.

The pore-type distribution provides insights into geological processes and implications for carbonate reservoir characterization. As illustrated in Fig. 16(b)–(d), the pore spaces in the target zone consist of a mixed system of reference pores and cracks, which align well with the fault distribution. The large proportion of reference pores (intergranular and intercrystalline pores) is typically a result of dolomitization reactions, calcite cementation, and dissolution of cements or matrix, which become the dominant gas storage spaces. On the other hand, cracks may be closely related to local tectonic activity and differential compaction,

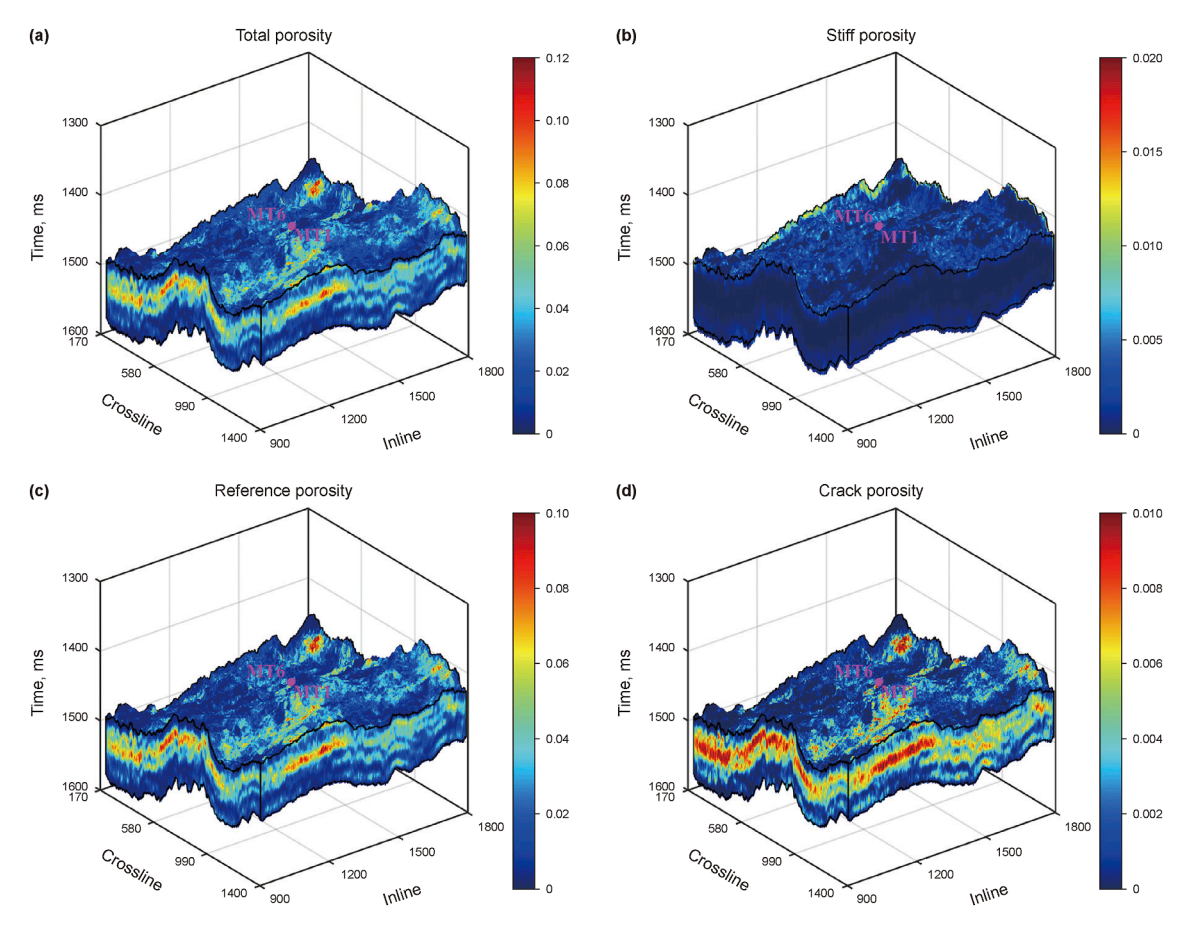


Fig. 16. 3D inversion results of pore types. (a) Total porosity; (b) stiff porosity; (c) reference porosity; (d) crack porosity.

enhancing porosity and permeability in carbonate reservoirs. It is worth noting that the inverted pore-type distribution is insufficient to capture the details of rock microstructures, and only represents the average properties of effective or homogenized medium. Thus, an integrated approach involving core descriptions, geological knowledge, well logs, and 3D seismic data is required to enhance reliability and increase confidence in pore-type assessment, ensuring a better understanding of pore structure characteristics.

In addition to elucidating the geological history, the pore-type distribution can also assist in detecting high-quality reservoirs. Generally, the presence of cracks significantly enhances reservoir permeability but reduces storage capacity. Stiff pores (vuggy and moldic pores) indicate large pore volumes but have poor transportability due to the disconnection between pores, greatly lowering natural gas production. In comparison, reference pores (intergranular and intercrystalline pores) correlate well with permeability and have relatively good storage capacity. Consequently, good-quality reservoirs should predominantly consist of stiff or reference pores to ensure high porosity, along with a certain number of cracks to ensure high permeability. Despite extensive studies aimed at establishing a reliable relationship between porosity and permeability (Cai et al., 2019; Khoshdel et al., 2022), the effects of pore type and porosity on permeability remain poorly understood. Therefore, future studies will focus on deriving a theoretical model that directly links pore type and porosity to rock permeability, thereby achieving more accurate permeability estimate.

#### 8. Conclusions

In this study, we developed a TPEM model for tight carbonate reservoirs, based on the extended Keys-Xu model and Gassmann's equation. The feasibility of this model was validated by comparing its estimations with laboratory data, which also helped determine the pore aspect ratios for each pore type. Using the calibrated model, we proposed a novel TPTI method that employs gridsearching method to simultaneously estimate the porosities of stiff pores, reference pores, and cracks. This method was applied to the Ordovician Majiagou Formation in the eastern Ordos Basin. The application of well-log data shows that the estimated reference porosity closely matches the logging interpretation results. Seismic inversion results further indicated that the Ma 4 member, the target interval, is characterized by a crack-pore type reservoir, where reference pores serve as the primary storage spaces, and cracks mainly act as essential pathways for oil and gas migration. These findings are consistent with logging evaluation results and gas testing reports. The proposed TPTI method not only provides an accurate characterization of the distribution of triple pore types in tight carbonate reservoirs but also successfully reveals the

microscopic mechanisms of hydrocarbon migration and accumulation. This method offers a theoretical foundation and technical support for characterizing pore structures in ultra-deep tight reservoirs using well logging and seismic data.

#### **CRediT authorship contribution statement**

Meng-Bo Zhang: Writing – original draft, Data curation, Conceptualization. Hao-Jie Pan: Writing – review & editing, Writing – original draft, Validation, Software, Methodology, Conceptualization. Yong-Gang Wang: Supervision, Project administration, Investigation, Data curation. Miao Du: Visualization, Validation, Software, Resources, Methodology, Investigation. Sheng-Juan Cai: Writing – review & editing, Validation, Supervision, Investigation. Feng Liu: Validation, Supervision, Resources, Investigation, Data curation. Mei-Xin Ju: Validation, Supervision, Investigation, Data curation.

#### **Declaration of competing interest**

The authors declare that they have no known competing financial interests or personal relationships that could have appeared to influence the work reported in this paper.

#### Acknowledgements

This work is supported by the National Engineering Laboratory for Exploration and Development of Low-Permeability Oil and Gas Fields (KFKT2023-20) and the National Natural Science Foundation of China (42104121). Miao Du and Meng-Bo Zhang have the same contributions to this work.

### Appendix A. Tensors $T_{ijij}$ and $T_{iijj}$

The tensor  $T_{ijkl}$  relates the uniform far-field strain field to the strain within the ellipsoidal inclusion (Wu, 1966), and Berryman (1980) gives the relevant scalars required for calculating P and Q as

$$T_{\text{iijj}} = 3F_1 / F_2, \tag{A3}$$

$$T_{ijij} - \frac{1}{3}T_{iijj} = \frac{2}{F_3} + \frac{1}{F_4} + \frac{F_4F_5 + F_6F_7 - F_8F_9}{F_2F_4},$$
 (A4)

where

$$F_1 = 1 + A \left[ \frac{3}{2} (f + \theta) - R \left( \frac{3}{2} f + \frac{5}{2} \theta - \frac{4}{3} \right) \right], \tag{A5}$$

$$\begin{split} F_2 &= 1 + A \bigg[ 1 + \frac{3}{2} (f + \theta) - \frac{R}{2} (3f + 5\theta) \, \bigg] + B(3 - 4R) + (A/2) (A \\ &+ 3B) (3 - 4R) \Big[ f + \theta - R \Big( f - \theta + 2\theta^2 \Big) \, \bigg], \end{split} \tag{A6}$$

$$F_3 = 1 + A \left[ 1 - \left( f + \frac{3}{2}\theta \right) + R(f + \theta) \right], \tag{A7}$$

$$F_4 = 1 + (A/4)[f + 3\theta - R(f - \theta)],$$
 (A8)

$$F_5 = A\left[-f + R\left(f + \theta - \frac{4}{3}\right)\right] + B\theta(3 - 4R),\tag{A9}$$

$$F_6 = 1 + A[1 + f - R(f + \theta)] + B(1 - \theta)(3 - 4R), \tag{A10}$$

$$F_7 = 2 + (A/4)[3f + 9\theta - R(3f + 5\theta)] + B\theta(3 - 4R),$$
 (A11)

$$F_8 = A \left[ 1 - 2R \frac{f}{2} (R - 1) + \frac{\theta}{2} (5R - 3) \right] + B(1 - \theta)(3 - 4R), \tag{A12}$$

$$F_0 = A[(R-1)f - R\theta] + B\theta(3-4R),$$
 (A13)

with A, B and R given by

$$A = G_{\rm in}/G_{\rm m} - 1 \tag{A14}$$

$$B = \frac{1}{3} (K_{in} / K_m - G_{in} / G_m)$$
 (A15)

and

$$R = (1 - 2\nu_{\rm m}) / 2(1 - \nu_{\rm m}), \tag{A16}$$

The functions  $\theta$  and f are given by

$$\theta = \begin{cases} \frac{\alpha}{(\alpha^2 - 1)^{3/2}} \left[ \alpha \left( \alpha^2 - 1 \right)^{1/2} - \operatorname{arccossh} \alpha \right] \\ \frac{\alpha}{(1 - \alpha^2)^{3/2}} \left[ \operatorname{arccos} \alpha - \alpha \left( \alpha^2 - 1 \right)^{1/2} \right] \end{cases}, \tag{A17}$$

for prolate and oblate spheroids, respectively, and

$$f = \frac{\alpha^2}{1 - \alpha^2} (3\theta - 2),\tag{A18}$$

Note that  $\alpha < 1$  for oblate spheroids and  $\alpha > 1$  for prolate spheroids.

#### References

Anselmetti, F.S., Eberli, G.P., 1993. Controls on sonic velocity in carbonates. Pure Appl. Geophys. 141, 287–323. https://doi.org/10.1007/BF00998333.

Anselmetti, F.S., Eberli, G.P., 1999. The velocity-deviation log: a tool to predict pore type and permeability trends in carbonate drill holes from sonic and porosity or density logs. AAPG (Am. Assoc. Pet. Geol.) Bull. 83 (3), 450–466. https://doi.org/10.1306/00AA9BCE-1730-11D7-8645000102C1865D.

Berryman, J., 1980. Long-wavelength propagation in composite elastic media II. Ellipsoidal inclusions. J. Acoust. Soc. Am. 68 (6), 1820–1831. https://doi.org/10.1121/1.385172

Cai, J.C., Zhang, Z.E., Wei, W., et al., 2019. The critical factors for permeability-formation factor relation in reservoir rocks: pore-throat ratio, tortuosity and connectivity. Energy 188, 116051. https://doi.org/10.1016/j.energy.2019.116051.

Chapman, M., 2003. Frequency-dependent anisotropy due to meso-scale fractures in the presence of equant porosity. Geophys. Prospect. 51 (5), 369–379. https:// doi.org/10.1046/j.1365-2478.2003.00384.x.

Chen, H.Z., Innanen, K.A., 2018. Estimation of fracture weaknesses and integrated attenuation factors from azimuthal variations in seismic amplitudes. Geophysics 83 (6), R711–R723. https://doi.org/10.1190/geo2018-0199.1.

Chichinina, T., Obolentseva, I., Gik, L., et al., 2009. Attenuation anisotropy in the linear-slip model: interpretation of physical modeling data. Geophysics 74 (5), WB165–WB176. https://doi.org/10.1190/1.3173806.

Du, M., Pan, H.J., Wei, C., et al., 2024. Simultaneous quantification of triple pore types in carbonate reservoirs using well logs and seismic data. Geophysics 89 (6), M211–M226. https://doi.org/10.1190/geo2023-0786.1.

Fournier, F., Pellerin, M., Villeneuve, Q., et al., 2018. The equivalent pore aspect ratio as a tool for pore type prediction in carbonate reservoirs. AAPG (Am. Assoc. Pet. Geol.) Bull. 102 (7), 1343–1377. https://doi.org/10.1306/10181717058.

Fu, J.H., Yu, Z., Li, C.S., Wang, W.B., Huang, Z.L., Wu, X.N., Wang, S.Y., 2021. New discovery and favorable areas of natural gas exploration in the 4th Member of Ordovician Majiagou Formation by Well Mitan 1 in the eastern Ordos Basin. Nat. Gas Industry 41, 17–27 (in Chinese).

Fu, J., Wu, X., Sun, L., et al., 2017. New understandings of the lithofacies paleogeography of the middle assemblage of Majiagou Fm in the Ordos Basin and its

- exploration significance. Nat. Gas. Ind. B 4 (4), 278–286. https://doi.org/10.1016/i.ngib.2017.08.011.
- Gassmann, F., 1951. Elastic waves through a packing of spheres. Geophysics 16 (4), 673–685. https://doi.org/10.1190/1.1437718.
- Guo, Z.Q., Li, X.Y., 2015. Rock physics model-based prediction of shear wave velocity in the Barnett Shale formation. J. Geophys. Eng. 12 (3), 527–534. https://doi.org/10.1088/1742-2132/12/3/527.
- Guo, Z.Q., Liu, C., Liu, X.W., et al., 2016. Research on anisotropy of shale oil reservoir based on rock physics model. Appl. Geophys. 13 (2), 382–392. https://doi.org/ 10.1007/s11770-016-0554-0.
- Guo, Z.Q., Qin, X.Y., Liu, C., 2023. Quantitative characterization of tight gas sandstone reservoirs using seismic data via an integrated rock-physics-based framework. Pet. Sci. 20 (6), 3428–3440. https://doi.org/10.1016/j. petsci.2023.09.003.
- Guo, Z.Q., Qin, X.Y., Zhang, Y.M., et al., 2021. Numerical investigation of the effect of heterogeneous pore structures on elastic properties of tight gas sandstones. Front. Earth Sci. 9, 641637. https://doi.org/10.3389/feart.2021.641637.
- He, H.Q., Guo, X.J., Zhao, Z.Y., et al., 2022. New understandings on gas accumulation and major exploration breakthroughs in subsalt Ma 4 member of Ordovician Majiagou Formation, Ordos Basin, NW China. Petrol. Explor. Dev. 49 (3), 489–501. https://doi.org/10.1016/S1876-3804(22)60041-7.
- Hill, R., 1952. The elastic behavior of a crystalline aggregate. Proc. Phys. Soc. 65 (5), 349–354. https://doi.org/10.1088/0370-1298/65/5/307.
- Keys, R.G., Xu, S., 2002. An approximation for the Xu–White velocity model. Geophysics 67, 1406–1414. https://doi.org/10.1190/1.1512786.
   Khoshdel, H., Javaherian, A., Saberi, M.R., et al., 2022. Permeability estimation using
- Khoshdel, H., Javaherian, A., Saberi, M.R., et al., 2022. Permeability estimation using rock physics modeling and seismic inversion in a carbonate reservoir. J. Petrol. Sci. Eng. 219, 1–16. https://doi.org/10.1016/j.petrol.2022.111128.
- Kumar, M., Han, D.H., 2005. Pore shape effect on elastic properties of carbonate rocks. In: 75th Annual International Meeting. SEG Expanded Abstracts, pp.1477–1481. https://doi.org/10.1190/1.2147969.
- Kuster, G.T., Toksöz, M.N., 1974. Velocity and attenuation of seismic waves in two-phase media: Part I. Theoretical formulations. Geophysics 39 (5), 587–606. https://doi.org/10.1190/1.1440450.
- Lai, J., Wang, S., Wang, G.W., et al., 2019. Pore structure and fractal characteristics of Ordovician Majiagou carbonate reservoirs in Ordos Basin, China. AAPG (Am. Assoc. Pet. Geol.) Bull. 103 (11), 2573–2596. https://doi.org/10.1306/ 02251917173.
- Li, H.B., Zhang, J.J., 2014. A differential effective medium model of multiple-porosity rock and its analytical approximations for dry rock. Chin. J. Geophys. 57 (6), 835–845. https://doi.org/10.1002/cjg2.20146 (in Chinese).
- Li, H.B., Zhang, J.J., Cai, S.J., et al., 2020. A two-step method to apply Xu–Payne multi-porosity model to estimate pore type from seismic data for carbonate reservoirs. Pet. Sci. 17, 615–627. https://doi.org/10.1007/s12182-020-00440-2.
- Mirkamali, M.S., Javaherian, A., Hassani, H., et al., 2020. Quantitative pore-type characterization from well logs based on the seismic petrophysics in a carbonate reservoir. Geophys. Prospect. 68 (7), 2195–2216. https://doi.org/10.1111/ 1365-2478.12989.
- Norris, A., 1985. A differential scheme for the effective moduli of composite. Mech. Mater. 4 (1), 1–16. https://doi.org/10.1016/0167-6636(85)90002-X.
- Saberi, M.R., 2020. Geology-guided pore space quantification for carbonate rocks. First Break 38 (3), 49–55. https://doi.org/10.3997/1365-2397.fb2020018.
- Sharifi, J., 2022. Intelligent pore type characterization: Improved theory for rock physics modelling. Geophys. Prospect. 70 (5), 921–937. https://doi.org/10.1111/1365-2478.13204.

- Sharifi, J., Mirzakhanian, M., Saberi, M.R., et al., 2018. Quantification of pore type system in carbonate rocks for rock physics modelling. In: 80th EAGE Conference and Exhibition, pp. 1–5. https://doi.org/10.3997/2214-4609.201800674.
- Sun, S.Z., Wang, H., Liu, Z., et al., 2012. The theory and application of DEM-Gassmann rock physics model for complex carbonate reservoirs. Lead. Edge 31 (2), 152–158. https://doi.org/10.1190/1.3686912.
- Sun, Y.F., Berteussen, K., Vega, S., et al., 2006. Effects of pore structure on 4D seismic Signals in carbonate reservoirs. In: 76th Annual International Meeting. SEG Expanded Abstracts, pp. 3260–3264. https://doi.org/10.1190/1.2370208.
- Teillet, T., Fournier, F., Zhao, L.X., et al., 2021. Geophysical pore type inversion in carbonate reservoir: integration of cores, well logs, and seismic data (Yadana field, offshore Myanmar). Geophysics 86 (3), B149–B164. https://doi.org/10.1190/geo2020-0486.1.
- Tian, H., Wang, G.W., Feng, Q., et al., 2020. Review and prospective of complex pore structure of carbonate reservoir. Sci. Technol. Eng. 20 (29), 11825–11833. https://doi.org/10.3969/j.issn.1671-1815.2020.29.002 (in Chinese).
- Wang, J.Q., Deng, J.X., Xu, Z.H., et al., 2024. Rock physics properties and influencing factors of subsalt carbonate reservoir of Ordovician Majiagou Formation in central Ordos Basin. Pet. Sci. 22 (1), 1–16. https://doi.org/10.1016/j.petsci.2024.05.024.
- Wang, P., Chen, X.H., Li, X.Y., et al., 2021. Analysis and estimation of an inclusion-based effective fluid modulus for tight gas-bearing sandstone reservoirs. IEEE Trans. Geosci. Rem. Sens. 60, 1–10. https://doi.org/10.1109/tgrs.2021.3099134.
- Wang, P., Cui, Y.A., Liu, J., 2022. Fluid discrimination based on inclusion-based method for tight sandstone reservoirs. Surv. Geophys. 43 (5), 1469–1496. https://doi.org/10.1007/s10712-022-09712-5.
- Weger, R.J., Eberli, G.P., Baechle, G.T., et al., 2009. Quantification of pore structure and its effect on sonic velocity and permeability in carbonates. AAPG (Am. Assoc. Pet. Geol.) Bull. 93 (10), 1297–1317. https://doi.org/10.1306/05270909001.
- Wei, X.S., Chen, H.D., Zhang, D.F., et al., 2017. Gas exploration potential of tight carbonate reservoirs: a case study of Ordovician Majiagou Formation in the eastern Yi-Shan slope, Ordos Basin, NW China. Petrol. Explor. Dev. 44 (3), 347–357. https://doi.org/10.1016/S1876-3804(17)30041-1.
- Wu, B.H., Chen, L., 2014. Optimizing calculation of multiple porosities in carbonates with petrophysics and rock physics integration strategy. In: 84th Annual International Meeting. SEG Expanded Abstracts, pp. 2819–2823. https://doi.org/10.1190/segam2014-0906.1.
- Wu, T.T., 1966. The effect of inclusion shape on the elastic moduli of a two-phase material. Int. J. Solids Struct. 2, 1–8. https://doi.org/10.1016/0020-7683(66) 90002-3.
- Xu, S.Y., Payne, M.A., 2009. Modeling elastic properties in carbonate rocks. Lead. Edge 28, 66–74. https://doi.org/10.1190/1.3064148.
- Zhang, J.J., Zeng, Q.C., Yin, X.Y., et al., 2021. Multiple-porosity variable critical porosity model and pore structure characterization. Chin. J. Geophys. 64 (2), 724–734. https://doi.org/10.6038/cjg2021M0675 (in Chinese).
- Zhang, X., Guo, Z.Q., Liu, C., 2024. Characterization of horizontal fractures in shale gas reservoirs using a rock-physics-based method integrated with SA-PSO algorithm and CNN. IEEE Trans. Geosci. Rem. Sens. 62, 5930414. https://doi.org/ 10.1109/TGRS.2024.3472057.
- Zhao, L.X., Nasser, M., Han, D.H., 2013. Quantitative geophysical pore-type characterization and its geological implication in carbonate reservoirs. Geophys. Prospect. 61, 827–841. https://doi.org/10.1111/1365-2478.12043.